Self-assembly of Metallic Copper Heterostructures Templated by Structural Anisotropy in Black Phosphorus Nanosheets

*[†]H.C. Nerl[1,2], [†]A. Pokle,[1,3], L. Jones[1,3], K. Müller-Caspary,[4] K.H.W. van den Bos[4], C. Downing,[3] E.K. McCarthy[3], N. Gauquelin,[4] Q.M. Ramasse[5,6,7], I. Lobato,[4] D. Daly,[3] J.C. Idrobo[8], S. Van Aert,[4] G. Van Tendeloo,[4] S. Sanvito,[1,2] J. N. Coleman,[1,2] *C. S. Cucinotta,[9] and *V. Nicolosi [2,3,10]

([†]equal contributions)
*Correspondence to: hcnerl@fhi-berlin.mpg.de; c.cucinotta@imperial.ac.uk; nicolov@tcd.ie

[1] School of Physics, Trinity College Dublin, Dublin 2, Ireland
[2] CRANN & AMBER, Trinity College Dublin, Dublin 2, Ireland
[3] Advanced Microscopy Laboratory, CRANN, Trinity College Dublin, Dublin 2, Ireland
[4] EMAT – University of Antwerp, Groenenborgerlaan 171, B-2020 Antwerp, Belgium
[5] SuperSTEM Laboratory, SciTech Daresbury Campus, Daresbury, WA4 4AD, UK
[6]School of Physics and [7]School of Chemical and Process Engineering, University of Leeds, Leeds LS2 9JT, UK
[8] Center for Nanophase Materials Sciences, Oak Ridge National Laboratory, Oak Ridge, TN 37831 USA
[9]TYC and Department of Chemistry, Imperial College London, UK
[10]School of Chemistry, Trinity College Dublin, Dublin 2, Ireland

The fabrication of two-dimensional systems for electronic devices is not straightforward with top-down low-yield methods often employed leading to irregular nanostructures and lower quality devices. Here we show a simple and reproducible method to trigger self-assembly of arrays of high aspect-ratio copper heterostructures templated by the structural anisotropy in black phosphorus nanosheets. Using quantitative atomic resolution aberration-corrected scanning transmission electron microscopy imaging, *in-situ* heating transmission electron microscopy and electron energy-loss spectroscopy we observed arrays of heterostructures forming at speeds exceeding 100 nm/s and displaying long-range order over microns. The controlled instigation of the self-assembly of the Cu heterostructures embedded in BP was achieved using conventional electron beam lithography combined with site specific placement of Cu nanoparticles. Density functional theory calculations were used to investigate the atomic structure and suggest a metallic nature of the Cu heterostructures grown in BP. These findings open new and exciting opportunities for next generation, self-assembling devices.

Unlike graphene, semiconductor few-layer black phosphorus (BP) exhibits a direct bandgap[1] leading to diverse electronic and thermal properties[2-11]. BP was first successfully synthesised under pressure over a century ago[12]. However, only has the recent successful exfoliation of monolayer BP [2, 4, 13, 14] led to its rediscovery for applications ranging from electronics, catalysis, sensors to biomedical drug delivery [15-33].

For many of these applications, there is a need for hybrid structures to combine the merits of low-dimensional materials for the design and fabrication of nanodevices by balancing requirements for electronic/electrical properties, improved stability and optical tenability. Multiple 2D materials, including BP, can be stacked vertically or stitched together to form in-plane heterojunctions, which combine the characteristics of the constituent compounds, thus allowing the tuning of electrical as well as optical properties [16, 34-36]. Another example of BP hybrid structures has been achieved by placing carbon nanotubes [37, 38] on top of BP to combine their properties. However, in general, Van der Waals heterostructures grow with a variable interlayer distance and twist angles between the layers [11, 12] two features that are almost impossible to control. This makes their properties varying from sample to sample and the design of composite nanostructures becomes unpredictable and, in the worst case, unreliable. Furthermore, in order to preserve the properties of the individual materials in the heterojunctions, the fabrication of atomically sharp interfaces is crucial. This, however, can be extremely challenging. Even though attempts to synthesize lateral interfaces have been made, roughness due to interfacial steps and traces of unwanted substitutional doping across the heterojunctions often result in a dilution or obliteration of the properties of the materials [13]–[16].

Here we propose a new hybrid nanostructure growth strategy. Our approach avoids the issues described above and uses a two-dimensional material to template the growth of novel hybrid structures.
This strategy is demonstrated here for the first time with BP, which is used to guide the self-assembly of highly directional Cu heterostructures templated by the underlying lattice structure. Our work uses atomic-resolution quantitative aberration-corrected scanning transmission electron microscopy (AC-STEM) imaging combined with simultaneous electron energy-loss spectroscopy (EELS) to demonstrate the *in-situ* self-assembly of Cu heterostructures in a BP nanosheet matrix. Using density functional theory (DFT) calculations we studied the thermodynamic stability and growth of the Cu heterostructures and investigated their electronic structure.

In situ formation of heterostructures templated by BP lattice

High-angle annular dark field (HAADF) STEM imaging in **fig.1a** shows the self-assembled high-aspect-ratio Cu structures as they formed through the contact of Cu nanoparticles dropped onto the BP nanosheets. The same growth mechanism was observed for both liquid exfoliated as well as mechanically exfoliated BP nanosheets. The Cu structure formation was studied using *in-situ* heating transmission electron microscopy (TEM) and it was found that when heated to 300˚C, arrays of the structures as shown in **fig.1b** form rapidly. The growth speed was observed to exceed 100 nm/sec (structures grew across the whole field of view

within the minimum microscope acquisition time). More details on the different stages of the heating experiment and the video showing the formation of the structures is shown in the supplementary information (**SI**), section **SI1** and video **V1** respectively. We expect the formation energy of these structures to strongly favour self-assembly as the BP was found to be an especially effective scavenger of any local Cu in the surroundings; this includes the self-formation using the Cu from the TEM support grid itself when heated even in the absence of specific Cu nanoparticle addition (also shown in **SI**). In all cases, the growth of the structures solely occurred along the [010] direction, as shown in the images in **fig.1a&b**. No growth was ever observed in any other direction. This strongly suggests that the Cu growth is templated by the lattice of the BP. The schematic of a BP nanosheet as seen along the [001] crystallographic direction shown in **fig.1c** illustrates the direction of the Cu structure growth (see **SI**, section **SI2** for more details on the BP lattice structure). In BP the P atoms join together to form a two-dimensional puckered sheet with natural channels along the [010] direction, forming adjacent hexagonal chairs in an orthorhombic arrangement [24]–[26]. A computational investigation showed the Cu atoms diffusing with a low energy barrier (ΔE=0.14eV) along the grooves of the BP lattice along the [010] direction (details in **SI**, section **SI5** for details on computational simulations), which further supports that the Cu growth is templated by the BP lattice.

Controlled initiation of self-assembly of Cu structures

Here we describe two techniques to successfully achieve a controlled seeding of Cu in the BP. In the first approach, Cu NPs were individually transferred using a micro-mechanical manipulator onto a mechanically exfoliated BP flake already deposited on a silicon wafer. Cu atom diffusion was then achieved by simply heating the system. The second and more controllable technique involved using electron beam lithography to directly evaporate Cu to specific sites on the exfoliated BP nanosheets, already deposited on a silicon substrate. Heating to 300˚C enabled Cu diffusion. With both techniques, we achieved control over the growth initiation sites as the growth was observed originating solely from the BP nanosheet areas where the Cu NPs had been deposited. More details on these methods can be found in the **SI**, section **SI3**.

High resolution imaging and analysis of the Cu structures

HAADF STEM imaging of the structures grown in the BP is displayed in **fig.1b,d&e** where various structures in a multi-layered BP nanosheet are shown in the simultaneous dark field (DF) and bright field (BF) images (**fig.1d** and **fig.1e** respectively). The high-resolution images **fig.1d&e** show that the pair of structures to the left-hand-side of the images appears to undulate in a regular manner but the individual structure on the right-hand side appears to be straighter in comparison. The undulations have been found to follow a regular pattern with ~2nm periodicity (see **SI**, section **SI4** for more details).

Atomic resolution imaging of BP in both the [001] and R17/-R17 orientations (with R17 and -R17 being equivalent in BP by symmetry as described in the SI, section **SI2**) revealed that the Cu structures are only 3-atoms-wide (as shown in **fig.2a-e** and **fig.2f-h** respectively). The interaction of Cu with phosphorus was found to be highly localized (**fig.2a** and section **SI 5**). Core-loss electron energy-loss spectroscopy (EELS) (**fig.2b-d)** confirmed both that the

structures are composed of Cu and that the separation between the Cu structures and the BP nanosheets is atomically sharp.

The structures also appear to be regularly spaced along [100] direction (in the direction perpendicular to the growth direction) as shown in **fig2g**. This spacing was found to be multiples of 0.45nm, which matches the theoretically calculated distance between the grooves in the [010] direction of the BP lattice (more details on the undulations as well as the spacing between structures can be found the **SI**, section **SI4**), again confirming that the growth is templated by the anisotropic geometry of the BP lattice.
DFT calculations showed that the diffusion of a Cu atom on a BP surface occurs interstitially, through a zigzag pathway joining the centres of the adjacent BP hexagonal chairs. Furthermore we found that the process leading to the formation of a Cu surface structure becomes more energetically favourable with increasing nanostructure length, which provides further computational support for the great speed of the structure formation we observed experimentally (for more details on the energetics and kinetics of Cu interaction with BP see **SI**, section **SI5**). Hence, the BP sheets provide the template for the Cu growth as shown by the combined evidence described above.
The undulations of the structure were clearly visible in atomic resolution STEM images as shown in the images in **fig.2**. In the thinner BP sheets, the Cu structures even exhibited undulations in the R17/-R17 orientation (**fig.2f**). The undulating pattern of the structures was found to vary in directionality across the structures. Structures 1&2 shown in **fig.2h** as well as structure 4 (which exhibits only very slight undulations) are of different chirality compared to structure 3. The structures also appear to introduce different steps into the different projections of the BP structure of the same thickness: structures 1-3 introduce a step, but structure 4 does not appear to do so (marked with a red dotted line in **fig.2h**). The same step difference was observed in the R17/-R17 orientation as shown in **fig.2e.** In both regions, the BP sheet adjacent to the Cu structures exhibits the same STEM intensity which indicates that the thickness is approximately constant (a quantitative STEM analysis will be presented below). This suggests that the observed difference in stepping behaviour is not a result of differing BP thicknesses. The observed differences in undulating patterns and step introduction could however result from different horizontal stacking of structures of different chirality and/or vertical offset between structures as well as from different Cu thicknesses or a combination of all. Occasionally, Cu structures that terminate in the BP sheet were observed (shown in **SI**). This further supports the suggestion that the Cu structures are indeed heterostructures of a certain thickness which appear to vary in thickness between different structures.

However, in order to confirm the thickness of the Cu structures as well as to study their physical properties and formation process, a structure model of the arrangement of Cu and P atoms within one period of undulation is needed. First, we developed an empirical structure model to provide information on the projected Cu structures by comparing image simulations quantitatively with calibrated experimental STEM images. In a second step, we employed comprehensive DFT simulations to discuss the physical properties for a catalogue of closest-match Cu structures.

Quantitative imaging of the heterostructures

HAADF STEM image-contrast quantification performed over a Cu//BP flake in its R17/-R17 direction was employed to study the precise thicknesses by quantitatively comparing experiment with simulations. [39, 40]

Since the structure of the BP is well known, the comparison of thickness-dependent STEM intensity simulations with calibrated experimental images allows for the accurate measurement of the sheet thickness in regions of pure BP. The average BP sheet thickness in the region shown in **fig. 3a** was measured to be 5.5 nm in the R17/-R17 orientation, the equivalent of 9 BP unit cells. This knowledge of the exact BP thickness was then employed to develop an empirical structure model for the Cu structure to consistently account for the relative contrast in the Cu sites compared to the BP sites. On first assessment, the significant additional contrast in the Cu sites compared to the BP sites in a nanosheet of 5.5nm thickness cannot be explained by the addition of an individual Cu nanowire. Hence experimental and computational evidence strongly suggests that the Cu structures forming in the BP are in fact 2D heterostructures. In order to confirm this hypothesis, the knowledge of the exact BP thickness and the periodicity of the Cu structure assessed by template matching (image shown in **fig.3c**) were used to develop the empirical model structure for the Cu heterostructure shown in **fig.3b**. The validity of this empirical model structure was assessed using dynamical multi-slice simulations with the MULTEM software [41] to obtain the simulated image shown in **fig.3d** which shows a close match to experiment in the R17/-R17 projection. The close match between the relative contrast in the electron microscopy projections and the image simulated from the empirical model structure suggests that the Cu structure is indeed a 2D heterostructure and not an individual nanowire of Cu. These 2D heterostructures are most likely composed of stacks of structures that interact with each other to form regular but chiral polymorph 2D heterostructures of Cu in the BP nanosheets composed of several layers of BP.

Armed with this knowledge we proceeded using density functional theory (DFT) calculations to study the nanoscopic, atomic and electronic structure of the Cu heterostructures.

Density functional theory (DFT) and image simulations of the Cu heterostructures

The chiral polymorphism of the observed experimental structure was confirmed by our DFT calculations which showed different metastable chiral polymorphs of width ranging from 0.365 nm to 0.375 nm, depending on the structure. We then simulated images using the calculated DFT structures to directly compare them to experimental electron micrographs (using the fast image simulation tool Prismatic STEM [42], see methods section for details of the simulation parameters).

The Cu heterostructure that most closely matched the experiment was also one of the computationally most stable, with a formation energy of 0.60 eV/Cu atom (T-S-3 structure in **SI**, **section SI5**). As observed in the experimental *in-situ* measurements, the DFT 2D heterostructure also forms along the natural BP growth channel in the [010] direction and extends transversally along the [001] direction. The DFT heterostructure results from the vertical alignment of three-atoms-thick Cu wires with a triangular cross section, growing

interstitially within BP layers as shown in **fig.4a**. Wires belonging to adjacent BP layers grow with an offset of one BP lattice parameter along the [010] direction, such that the heterostructure, appears continuous along the growth path, when observed along the [001] direction, while gaps are exposed when the structure is rotated by 17˚ (or by -17 ˚depending on the chirality of the heterostructure).

As described earlier, R17 and –R17 orientations of clean BP are equivalent by symmetry, but the chiral nature of the Cu heterostructures investigated causes this symmetry to be broken. Without knowledge of the exact 3D structure there is no way to distinguish between both orientations experimentally. However, it is possible to observe the DFT structures from different orientations and compare the simulated EM projections of the DFT structure in the R17 and -R17 orientations. When doing so, it becomes evident that the simulated images of the same chiral structure in the R17 and -R17 orientations are indeed distinct (as shown in **fig.4a-b,** additional image simulations of all orientations can be found in the **SI**, **Fig.SI14 and Fig.SI15**).

The simulated images of the T-S-3 structure are shown in **fig.4b,** in **i)** [001] and **iii)** -R17 orientations respectively. The corresponding experimental electron micrographs are shown in **ii)** and **iv)** respectively. Several different polymorphs of the T-S-3 structure were computationally observed, mainly differing for the chirality of the structure and the disposition and/or density of the atoms along the central axis of Cu heterostructure. The formation energies of such polymorphs are very similar, and range from 0.6 to 0.7 eV/Cu atom (see **SI**, section **SI6:** T structures in table **SI.T1**).

To computationally confirm that the Cu structure is indeed a 2D heterostructure and not an individual Cu nanowire, we separately simulated the isolated nanowire intercalated within the BP, and found out that, although thermodynamically viable, its formation within BP (formation energy of ~0.27 eV/Cu atom) is less favourable than the formation of the 2D nanostructure.
In addition, both the same undulations in the simulated images as observed experimentally, and the continuity of the Cu heterostructure as observed from [001] direction are fully recovered only when relaxing the replicated nanowire unit to form the heterostructure (**SI**, **fig.SI14** and **fig.SI15**).
Furthermore, we found that the image simulations of the EM projections of the DFT structure reproduce the step in the BP lattice in the –R17 but not in the R17 orientation as observed experimentally. These findings prove that the chiral nature of the Cu heterostructure is at the origin of the conformational variations observed experimentally.

Besides the most stable structure and its chiral polymorphs, our computational results show that a number of other metastable heterostructures can also be formed (with formation energies ranging from 0.5 to 0.2 eV/Cu atom), either composed by intercalated nanotubes with hexagonal cross-sections, or by nanowires with pentagonal or irregular cross-sections. The Cu atoms in these structures partially occupy substitutional positions, after a dissociative

processes leading to the release of P atoms. (A full catalogue of 2D heterostructures and the corresponding image simulations can be found in the **SI section SI6.**)

The analysis of the density of states of the T-S-3 structure (see **fig.4c**) suggests that the heterostructure is metallic. This is proven by a densification of the density of states around the Fermi level of the decorated system, with Bloch states and charge density localised around the wire (see **SI** section **SI5** for more details). This metallic character is present in all the metastable nanostructures observed computationally. An overlap of Cu and P centred states localised around the wire is also observed at all energies. This metallic nature of the Cu heterostructures in BP is of great interest for potentially using BP in nanodevice fabrication applications. As stated, because several other structures of similar formation energy could also form, there may be other electronic and structural variations of these wires, and a further study of this is planned.

Initiating the self-assembly of the metallic Cu heterostructures *in situ* in the BP nanosheets and thereby producing a hybrid material represents a novel way to fabricate nanodevices. Issues occurring during conventional fabrication of hybrid structures, including uncontrollable effects of stacking and relative orientation of materials, unwanted substitutional doping across heterostructures and interface roughness are thereby elegantly avoided using the approach described here. Moreover, controlled seeding of copper in BP is achievable with e-beam lithography, a standard technique used in the semiconducting industry which is readily scalable. Importantly, this can enable the use of existing technology and hardware to fabricate and design future BP-based electronic devices. The addition of the Cu heterostructures to the BP sheets is expected to further enhance the already existing, highly desirable directional anisotropy in optical and electrical properties inherent to BP and further studies of this are planned. The growth procedure has the potential to be used with other metals and 2D substrates and therefore represents a versatile fabrication protocol. This opens new and exciting opportunities for next generation, self-assembling devices.

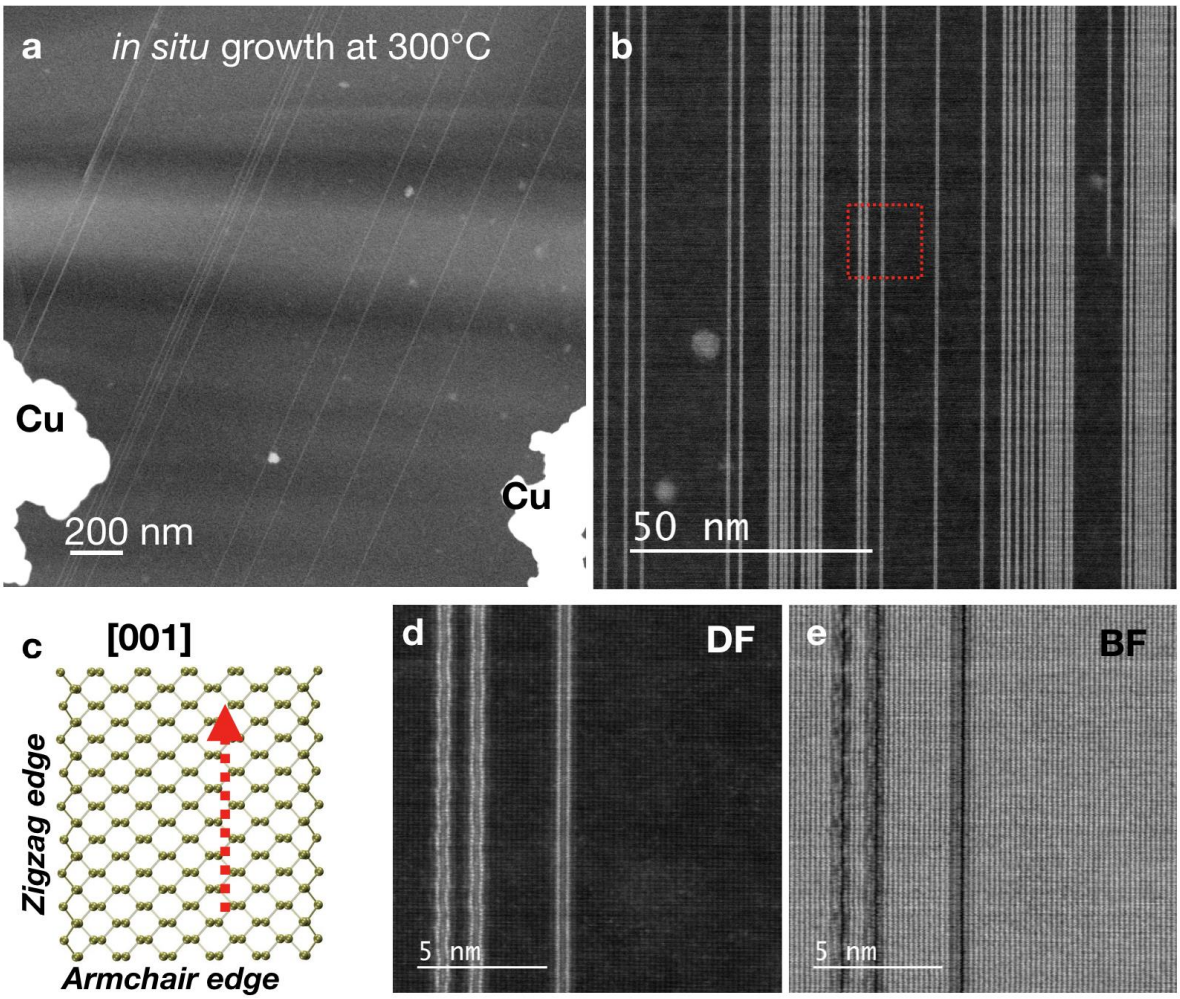

Figure 1: Self-assembly of Copper (Cu) heterostructures of high aspect ratio templated by the Black Phosphorus (BP) lattice. a) *High-angle annular dark field (HAADF) Scanning Transmission Electron Microscopy (STEM) image of the heterostructures formed during in situ heating to 300C. The Cu heterostructures were found to form rapidly, with formation speed >100 nm/sec.* ***b)*** *Large arrays of parallel Cu heterostructures in the BP were found to self-assemble.* ***c)*** *Atomic model of a BP nanosheet viewed along the [001] crystallographic directions; the red arrow illustrates the direction of the Cu heterostructure growth.* ***d)*** *High resolution HAADF STEM image and* ***e)*** *corresponding Bright Field (BF) image of the same region as marked in red in b), showing a pair of undulating Cu lines and a third straighter line of Cu.*

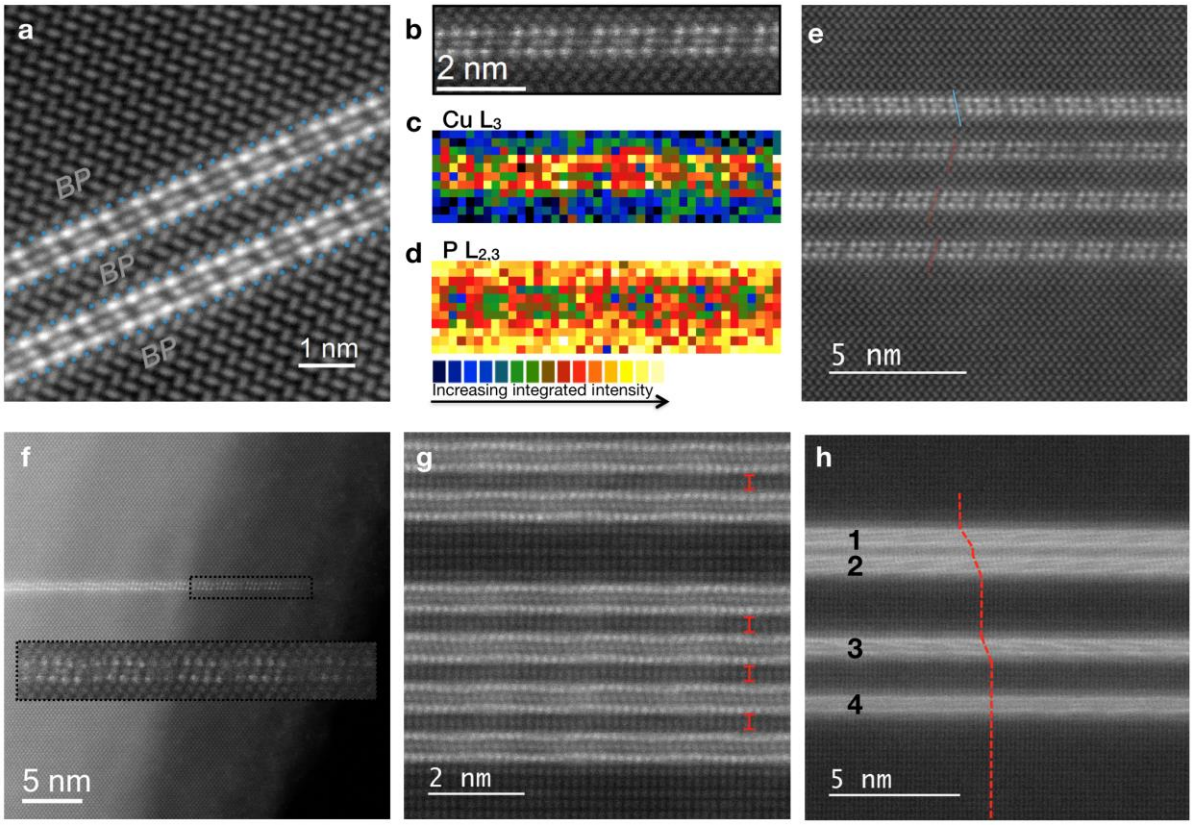

Figure 2: ***High-resolution High-angle Annular Dark Field (HAADF) Scanning Transmission Electron Microscopy (STEM) imaging and analysis of Copper (Cu) structures in Black Phosphorus (BP) nanosheets.***

HAADF STEM imaging and analysis of the BP in ***a-e)*** *the* R17/-R17 *orientation and* ***f-h)*** *the [001] orientation revealed that the Cu structures are only 3-atoms-wide.*

a)* *The interaction of Cu with phosphorus was found to be highly localized (interface marked with blue dotted line).* ***b-d)*** *Core-loss electron energy-loss spectroscopy (EELS) confirmed that the structure is composed of Cu.* ***e)*** *In the EM projections of the Cu in the BP, different stepping behaviour was observed for different Cu structures (marked with a dotted red line and a continuous blue line) by the Cu in the* R17/-R17 *orientation.* ***f)*** *In the thinner BP sheets, the Cu structures exhibit undulations in the R17 orientation as well. Also, differences in the relative intensities of the Cu in the structures in thinner BP sheets become apparent as shown as an inset in* ***f)*** *when compared to the thicker regions shown in* ***e. g)*** *The Cu structures exhibit undulating patterns and the structures are regularly spaced (see red markings).* ***h)*** *The undulating pattern varied across the structures. Here the structures 1&2 as well as structure 4 (which exhibits only a very slight undulating pattern) are of different chirality compared to structure 3. As in the projections of the* R17/-R17 *orientation, the Cu structures were found to introduce a different step into the BP in regions of the same thickness. Structures 1-3 introduce a step, but structure 4 does not (marked in red dotted line). (*was averaged using rigid registration from a series of consecutive images [35])*

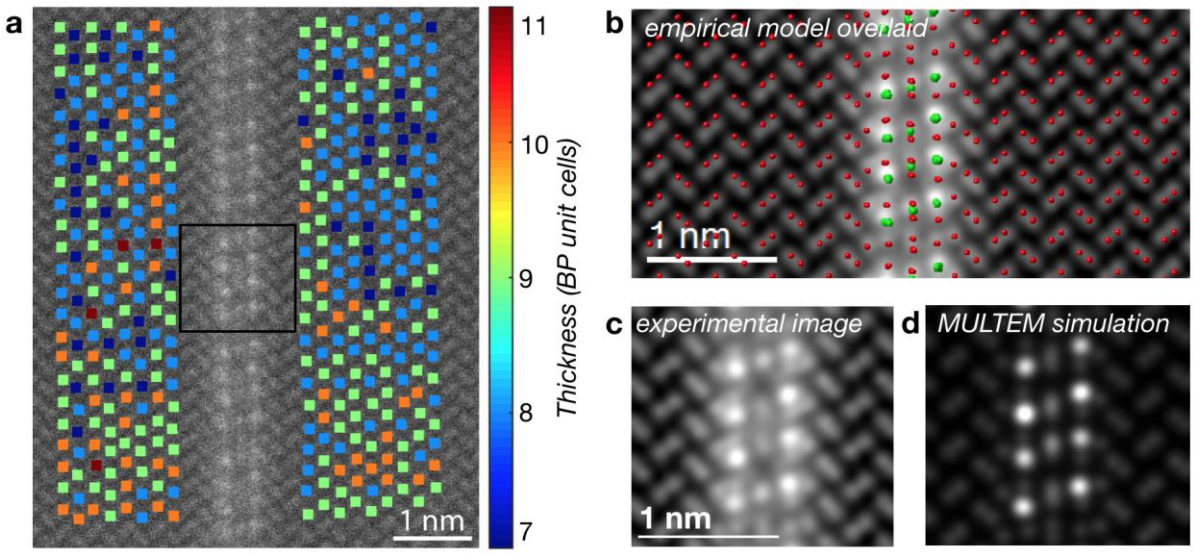

Figure 3: Image quantification for determination of Copper (Cu) heterostructures thickness in the BP. a) *High Angle Annular Dark Field (HAADF) Scanning transmission electron microscopy (STEM) image quantification performed over a Cu//BP flake in its* R17/-R17 *direction. A precise knowledge of the thickness or the number of layers is required in order to simulate the HAADF STEM images. The thickness in BP was found to be 9 unit cells, or ~5.5nm. ***b)** Empirical model structure obtained to estimate thickness of the Cu in the BP lattice overlaid over template-matched experimental STEM image of Cu structures in BP nanosheets. ***c)** Detail from template-matched experimental STEM image of Cu structure in BP nanosheets next to **d)** simulated image obtained from the empirical model structure using MULTEM. (* image was frame-averaged [35], then template-matched, then denoised)*

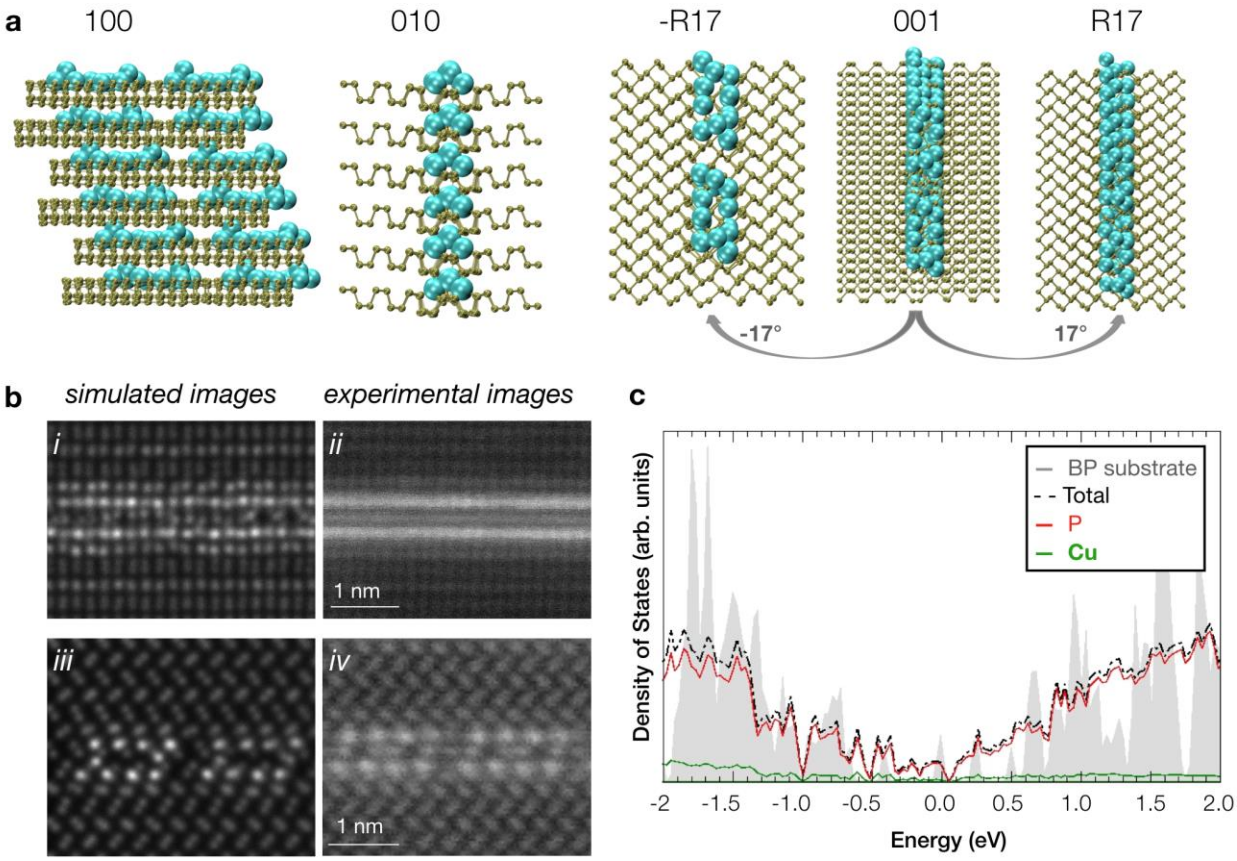

Figure 4: ***Using an iterative combination of density functional theory (DFT) and image simulation, potential stable and energetically favourable structures of the Copper (Cu) heterostructures in the Black Phosphorus (BP) nanosheets were investigated.***

a*) Ball and stick representation of the structure that was found to provide the closest match with experiment in orientations [100], [010], -R17, [100] and R17. Green and cyan balls represent P and Cu atoms, respectively.* ***b)*** *Simulated images* of the structure shown in* ***i)*** *[001] orientation and* ***iii)*** *-R17 orientation and compared to experimental STEM images in the same orientation shown in* ***ii)*** *and* ***iv)*** *respectively.* ***c)*** *Density of states (DOS), of the structure as shown in* ***a)*** *represented with a dashed black line, suggests that the heterostructure in the BP nanosheet is metallic. (*using the Prismatic STEM image simulation tool.) the DOS of the clean BP substrate and the Projected DOS on P and Cu atoms of the structure are also represented in red and green, respectively.*

Acknowledgement
The authors acknowledge support from the European Research Council (ERC Starting Grant 2DNanoCaps, ERC TC2D, ERC CoG 3D2DPrint, ERC CoG Picometrics), FP7 ITN (MoWSeS), SFI (PIYRA and AMBER) and EPSRC (EP/P033555/1). Most of the imaging/analysis for this project was carried out at the Advanced Microscopy Laboratory (AML) at the AMBER centre, CRANN Institute www.tcd.ie/crann/aml/, Trinity College Dublin, Ireland. AML is an SFI supported imaging and analysis centre. K.M.-C., KH.W.v.d.B, I.L., N.G., S.V.A., and G.V.T. acknowledge support from the Research Foundation Flanders (FWO, Belgium) and the GOA project "Solarpaint" of the University of Antwerp. The Qu-Ant-EM microscope was partly funded by the Hercules fund from the Flemish Government. JCI acknowledges support from the Center for Nanophase Materials Sciences, which is a DOE Office of Science User Facility. We thank Julia Kremer and Akshara Verma (CRANN, Trinity College Dublin) for their assistance using the Temescal. SuperSTEM is the U.K. National Research Facility for Advanced Electron Microscopy, supported by the Engineering and Physical Sciences Research Council (EPSRC). All the calculations were performed using the ARCHER, UK, National Supercomputing Service (http://www.archer.ac.uk, via our membership of the UK's HEC Materials Chemistry Consortium, which is funded by EPSRC (EP/R029431)), and the Kelvin and Boyle clusters, maintained by the Trinity Centre for High Performance Computing (project id: HPC_16_00932, these clusters were funded through grants from Science Foundation Ireland).

Author Contributions
HCN wrote the manuscript with all authors contributing. HCN and AP analysed the data. CSC supervised the theoretical modelling and performed the DFT calculations with contribution from SS. HCN and LJ performed the image simulations. AP and EKM performed the EBL for control growth mechanism. KMC, KHWB, IL, NG, SVA and GVT performed the quantitative STEM experiments, analyses, simulations, and EELS analysis. AP acquired HAADF STEM images. QR and JCI performed HAADF STEM imaging and EELS experiments. DD and AP performed the copper transfer technique using FIB needle. JC contributed to the initial experiments. VN guided and supervised the project.

Competing interests
The authors declare no competing interests.

Methodology
Samples: The black phosphorus was purchased from Smart Elements (Art. Nr. 003933), and crystals were stored in a glove box (MBraun) to avoid degradation (H_2O and O_2 levels below 0.1 ppm). The mechanical exfoliation was carried out using NITTO blue tape (BT-150E-CM) inside the glove box. Liquid-phase exfoliation was carried out using isopropyl alcohol (IPA) as a solvent and sonication using a sonic tip (Fisher Scientific) for 4 hrs at 60% amplitude.[43] The obtained dispersions were centrifuged in a Heraeus Multifuge X1 Centrifuge at 3000 rpm for 90 minutes, followed by the separation of the supernatant from the non-exfoliated material. The exfoliated sheets were deposited on TEM holey carbon 200

mesh Cu grids purchased from SPI Supplies. Initially the wire growth was achieved by thermally treating the TEM grids in a vacuum oven (2×10^{-3} mbar) kept at 110°C for 5 days. The thermal treatment could also be achieved using a hot plate (IKA RCT basic) kept at 300°C for 5 min.

Growth of Copper heterostructures: For the controlled growth study, we used two different approaches: First, we drop-cast Cu nanoparticles on an SEM stub and then lifted them by Coulomb interaction using a fine needle (Picoprobe - GGB Industries controlled by Kleindiek-nanotechnik) in a Carl Zeiss Auriga FIB, operated at 5 kV. This way we could transfer particles onto exfoliated BP flakes deposited atop a silicon wafer (University Wafer).
The second methodology involved first exfoliating the BP nanosheets and transferring them onto a silicon wafer, followed by lithography using a Raith beam blanking system on a Carl Zeiss Supra 40 SEM and then by e-beam metal evaporation using a Temescal. More details on both growth procedures can be found in the **SI**.

Microscopy: Scanning Electron Microscopy (SEM) images of the controlled growth study were acquired using a Carl Zeiss Ultra operated at 5 kV. Aberration-corrected STEM (AC-STEM) HAADF imaging and EELS were carried out in a NION UltraSTEM200, operated at 60kV: for these experiments, the probe convergence semi-angle was 35mrad with a probe current of 35pA, resulting in a probe size of 1.2Å. Further imaging was carried out in a Nion UltraSTEM100MC 'Hermes'[44], also operated at 60kV: for these experiments, the probe convergence semi-angle was 31mrad with a probe current of 50pA, resulting in a probe size of 1Å. The HAADF detector inner and outer angles were calibrated as 85mrad and 185mrad respectively. Both microscopes are fitted with a Gatan Enfinium spectrometer for EELS. *In-situ* heating measurements were performed on a S/TEM FEI TITAN 80-300, operated at 300kV using a DENS wildfire holder. It is based on a Micro-Electro-Mechanical System (MEMS), controlling the temperature environment locally on the device by 4-point-probe. The temperature was initially varied from room temperature to 300°C at 50°C interval and kept at 300°C for 65 min. The temperature was then raised to 500°C with 50°C interval. The mechanically exfoliated BP was placed over the MEMS electron transparent windows and Cu nanoparticles (Sigma Aldrich 774111-5G) were drop-cast over it.

Image processing: The HAADF STEM image shown **fig.2b** was frame averaged and the image shown in **fig.3b** was frame-averaged [45], then template-matched, then denoised.[45]

EELS processing: Digital Micrograph was used to perform the EELS and STEM analysis. Principal Component Analysis (Multivariate Statistical Analysis from the Interdisciplinary Centre for Electron Microscopy (CIME) using 60 components were used for de-noising the STEM EELS maps shown in **fig.2**.[46]

Density functional theory: The DFT approach was applied as implemented in the CP2K code (www.cp2k.org). The CP2K Kohn and Sham orbitals were expanded in a mixed Gaussian (double-ζ plus polarization, DZVP) and plane-waves basis set. A 600 Ryd energy cut-off

was used for the plane-wave expansion of the electronic density. Tether and Goedecker-type pseudopotentials were used for all atoms, and Brillouin Zone integration was restricted to the Γ-point. The geometry and simulation cell were relaxed until the maximum force on each atom was less than 0.01 eV/Å. The PBE [47] exchange and correlation functional was used with a Van der Waals correction at the Grimme-D3 level [48] The Nudged Elastic Band (NEB) approach in its climbing image implementation was used to evaluate energy barriers along the Cu diffusion pathway heterostructure [49, 50]. Adsorption energies per Cu atom were evaluated as $\Delta E = (E_{BP} + nE_{Cu} - E_{Cu@BP} - n'E_P)/n$, where E_{BP} is the energy of the reference bulk BP slab, E_{Cu} is the chemical potential of a Cu atom (as taken from a reservoir represented by a 841 atoms Cu cluster), $E_{Cu@BP}$ is the energy of the decorated BP slab, *n* is the number of the adsorbed Cu atoms (N_{Cu} in table SI13 in SI) and *n'* the number of P atoms that have been released (P_{subst} in table **SI.T1** in **SI**). EP is the energy of a P atom, taken from a reservoir represented by the ideal BP bulk reference. More detail about the modelling of the interstitial periodical 2D heterostructures within BP is reported in **SI**.

Quantitative HAADF STEM: Quantitative STEM imaging was carried out at the FEI X-Ant-EM Titan class microscope at EMAT (Antwerp), which is equipped with an aberration corrector for the probe-forming system. The microscope was operated at 120keV primary energy and HAADF STEM images were acquired with a Fischione Model 3000 detector operated in its linear range, with acceptance angles of 46 to 215 mrad. Measured intensities were normalised to the incident beam intensity and compared to simulations employing the MULTEM software, which took the inhomogeneous detector sensitivity and partial spatial coherence into account. Thermal diffuse scattering was simulated with the frozen phonon model in an Einstein approximation using 20 phonon configurations. Statistical parameter estimation theory was employed as implemented in the StatSTEM software [34] to model the intensity distribution of each atomic column with a Gaussian in both simulation and experiment. This yields the integral scattered intensity of an atomic column, the scattering cross-section, which increases monotonically with specimen thickness. In order to improve the precision, we measured the cross-section of a P-dumbbell and compared with its simulated counterpart to determine the specimen thickness in **Fig. 3a**.

Further image simulations: Faster, less comprehensive image simulations of BP were performed using the Prismatic Software for STEM simulation.[42] Settings used: 1 frozen phonon per simulation for simulations shown in **SI**, 5 frozen phonons for the main paper (when directly comparing for the same structure, only slight improvements in noise-levels were observed when comparing images generated using between 1 up to 20 frozen phonons); potential bound = 0.3Å; Pixel size = 0.1x0.1Å. Images were generated for outer detector angles up to 200mrad. A source size of 0.8Å was added as well as a realistic noise level using a Matlab routine based on a Poisson distribution function.

References

1. Castellanos-Gomez, A., et al., *Isolation and characterization of few-layer black phosphorus.* 2d Materials, 2014. **1**(2).
2. Xia, F., H. Wang, and Y. Jia, *Rediscovering black phosphorus as an anisotropic layered material for optoelectronics and electronics.* Nat Commun, 2014. **5**: p. 4458.
3. Das, S., et al., *Tunable transport gap in phosphorene.* Nano Lett, 2014. **14**(10): p. 5733-9.
4. Liu, H., et al., *Phosphorene: an unexplored 2D semiconductor with a high hole mobility.* ACS Nano, 2014. **8**(4): p. 4033-41.
5. Liu, H., et al., *Semiconducting black phosphorus: synthesis, transport properties and electronic applications.* Chem Soc Rev, 2015. **44**(9): p. 2732-43.
6. Wang, X., et al., *Highly anisotropic and robust excitons in monolayer black phosphorus.* Nature Nanotechnology, 2015. **10**: p. 517.
7. Favron, A., et al., *Photooxidation and quantum confinement effects in exfoliated black phosphorus.* Nature Materials, 2015. **14**: p. 826.
8. Luo, Z., et al., *Anisotropic in-plane thermal conductivity observed in few-layer black phosphorus.* Nature Communications, 2015. **6**: p. 8572.
9. Doganov, R.A., et al., *Transport properties of pristine few-layer black phosphorus by van der Waals passivation in an inert atmosphere.* Nature Communications, 2015. **6**: p. 6647.
10. Zhang, L. and Y. Hao, *Electronic and optical responses of quasi-one-dimensional phosphorene nanoribbons to strain and electric field.* Scientific Reports, 2018. **8**(1): p. 6089.
11. Miao, X.C., et al., *Layer-Dependent Ultrafast Carrier and Coherent Phonon Dynamics in Black Phosphorus.* Nano Letters, 2018. **18**(5): p. 3053-3059.
12. Bridgman, P.W., *Two New Modifications of Phosphorus.* Journal of the American Chemical Society, 1914. **36**(7): p. 1344-1363.
13. Brent, J.R., et al., *Production of few-layer phosphorene by liquid exfoliation of black phosphorus.* Chemical Communications, 2014. **50**(87): p. 13338-13341.
14. Hanlon, D., et al., *Liquid exfoliation of solvent-stabilized few-layer black phosphorus for applications beyond electronics.* Nature Communications, 2015. **6**: p. 8563.
15. Buscema, M., et al., *Photovoltaic effect in few-layer black phosphorus PN junctions defined by local electrostatic gating.* Nature Communications, 2014. **5**: p. 4651.
16. Deng, Y., et al., *Black phosphorus-monolayer MoS2 van der Waals heterojunction p-n diode.* ACS Nano, 2014. **8**(8): p. 8292-9.
17. Li, L., et al., *Black phosphorus field-effect transistors.* Nature Nanotechnology, 2014. **9**: p. 372.
18. Churchill, H.O.H. and P. Jarillo-Herrero, *Phosphorus joins the family.* Nature Nanotechnology, 2014. **9**: p. 330.
19. Buscema, M., et al., *Fast and Broadband Photoresponse of Few-Layer Black Phosphorus Field-Effect Transistors.* Nano Letters, 2014. **14**(6): p. 3347-3352.
20. Yuan, H., et al., *Polarization-sensitive broadband photodetector using a black phosphorus vertical p–n junction.* Nature Nanotechnology, 2015. **10**: p. 707.
21. Youngblood, N., et al., *Waveguide-integrated black phosphorus photodetector with high responsivity and low dark current.* Nature Photonics, 2015. **9**: p. 247.

22. Perello, D.J., et al., *High-performance n-type black phosphorus transistors with type control via thickness and contact-metal engineering.* Nature Communications, 2015. **6**: p. 7809.
23. Wang, L., et al., *Synthesis of hybrid nanocomposites of ZIF-8 with two-dimensional black phosphorus for photocatalysis.* Rsc Advances, 2016. **6**(73): p. 69033-69039.
24. Shao, J., et al., *Biodegradable black phosphorus-based nanospheres for in vivo photothermal cancer therapy.* Nature Communications, 2016. **7**: p. 12967.
25. Tao, W., et al., *Black Phosphorus Nanosheets as a Robust Delivery Platform for Cancer Theranostics.* Advanced Materials, 2017. **29**(1).
26. Zheng, S.J., et al., *Acoustically enhanced photodetection by a black phosphorus-MoS2 van der Waals heterojunction p-n diode.* Nanoscale, 2018. **10**(21): p. 10148-10153.
27. Venuthurumilli, P.K., P.D. Ye, and X.F. Xu, *Plasmonic Resonance Enhanced Polarization-Sensitive Photodetection by Black Phosphorus in Near Infrared.* Acs Nano, 2018. **12**(5): p. 4861-4867.
28. Liu, C.L., et al., *Top-gated black phosphorus phototransistor for sensitive broadband detection.* Nanoscale, 2018. **10**(13): p. 5852-5858.
29. Gao, J.B., et al., *Carrier Transport Dynamics in High Speed Black Phosphorus Photodetectors.* Acs Photonics, 2018. **5**(4): p. 1412-1417.
30. Yang, B.W., et al., *2D-Black-Phosphorus-Reinforced 3D-Printed Scaffolds:A Stepwise Countermeasure for Osteosarcoma.* Advanced Materials, 2018. **30**(10).
31. Li, C., et al., *Synthesis of Crystalline Black Phosphorus Thin Film on Sapphire.* Advanced Materials, 2018. **30**(6).
32. Gao, G.Y., et al., *Tunable Tribotronic Dual-Gate Logic Devices Based on 2D MoS2 and Black Phosphorus.* Advanced Materials, 2018. **30**(13).
33. Xu, Z.-L., et al., *Exceptional catalytic effects of black phosphorus quantum dots in shuttling-free lithium sulfur batteries.* Nature Communications, 2018. **9**(1): p. 4164.
34. Liu, Y., et al., *Tailoring sample-wide pseudo-magnetic fields on a graphene–black phosphorus heterostructure.* Nature Nanotechnology, 2018.
35. Huber, M.A., et al., *Femtosecond photo-switching of interface polaritons in black phosphorus heterostructures.* Nature Nanotechnology, 2017. **12**(3): p. 207-+.
36. Chen, X., et al., *High-quality sandwiched black phosphorus heterostructure and its quantum oscillations.* Nature Communications, 2015. **6**: p. 7315.
37. Haghighat-Shishavan, S., et al., *Strong, persistent superficial oxidation-assisted chemical bonding of black phosphorus with multiwall carbon nanotubes for high-capacity ultradurable storage of lithium and sodium.* Journal of Materials Chemistry A, 2018. **6**(21): p. 10121-10134.
38. Bat-Erdene, M., et al., *Efficiency Enhancement of Single-Walled Carbon Nanotube-Silicon Heterojunction Solar Cells Using Microwave-Exfoliated Few-Layer Black Phosphorus.* Advanced Functional Materials, 2017. **27**(48).
39. LeBeau, J.M., et al., *Quantitative Atomic Resolution Scanning Transmission Electron Microscopy.* Physical Review Letters, 2008. **100**(20): p. 206101.
40. Rosenauer, A., et al., *Measurement of specimen thickness and composition in Al(x)Ga(1-x)N/GaN using high-angle annular dark field images.* Ultramicroscopy, 2009. **109**(9): p. 1171-1182.
41. Lobato, I. and D. Van Dyck, *MULTEM: A new multislice program to perform accurate and fast electron diffraction and imaging simulations using Graphics Processing Units with CUDA.* Ultramicroscopy, 2015. **156**: p. 9-17.

42. Ophus, C., *A fast image simulation algorithm for scanning transmission electron microscopy.* Adv Struct Chem Imaging, 2017. **3**(1): p. 13.
43. Hernandez, Y., et al., *High-yield production of graphene by liquid-phase exfoliation of graphite.* Nat Nanotechnol, 2008. **3**(9): p. 563-8.
44. Krivanek, O.L., et al., *Monochromated STEM with a 30 meV-wide, atom-sized electron probe.* Microscopy, 2013. **62**(1): p. 3-21.
45. Jones, L., et al., *Smart Align-a new tool for robust non-rigid registration of scanning microscope data.* Advanced Structural and Chemical Imaging, 2015. **1**.
46. Lucas, G., et al., *Multivariate statistical analysis as a tool for the segmentation of 3D spectral data.* Micron, 2013. **52-53**: p. 49-56.
47. Perdew, J.P., K. Burke, and M. Ernzerhof, *Generalized gradient approximation made simple.* Physical Review Letters, 1996. **77**(18): p. 3865-3868.
48. Grimme, S., et al., *A consistent and accurate ab initio parametrization of density functional dispersion correction (DFT-D) for the 94 elements H-Pu.* J Chem Phys, 2010. **132**(15): p. 154104.
49. Henkelman, G., B.P. Uberuaga, and H. Jonsson, *A climbing image nudged elastic band method for finding saddle points and minimum energy paths.* Journal of Chemical Physics, 2000. **113**(22): p. 9901-9904.
50. Henkelman, G. and H. Jonsson, *Improved tangent estimate in the nudged elastic band method for finding minimum energy paths and saddle points.* Journal of Chemical Physics, 2000. **113**(22): p. 9978-9985.

Supplementary Information

Self-assembly of Metallic Copper Heterostructures Templated by Structural Anisotropy in Black Phosphorus Nanosheets

SI 1 Ex-situ and In-situ Heating Experiments

To investigate the growth process, we performed controlled *in-situ* heating Transmission Electron Microscopy (TEM). For this experiment, Black Phosphorous (BP) was mechanically exfoliated and transferred onto a Microelectromechanical Systems (MEMS) chip. Copper (Cu) nanoparticles were dispersed in isopropyl alcohol (IPA) and carefully drop-cast onto the BP flakes on the MEMS chip. Video **V1** shows the Cu structure growth in real time, when a temperature of 300 °C was applied to the system (scanning TEM images were acquired at 1fps and the image sequences collated to produce the video).

Snapshots at different time points of the video are shown in **fig.SI2**. The diffusion of the Cu atoms is clearly starting from the Cu nanoparticles. Using this data, the speed of the assembly growth was calculated at temperatures of 300 °C. Three different heterostructure growths were analysed to obtain the growth rates. The orange dotted line in **fig.SI1** marks the starting point from which the measurements were taken to the end point for the growth, marked with a blue dotted line.

- **Fig.SI1 (a & b)**: 750 nm in maximum 08 sec = 93.75 nm/sec.
- **Fig.SI1 (c & d)**: 502 nm in maximum 05 sec = 104.4 nm/sec.
- **Fig.SI1 (e & f)**: 1069 nm in maximum 10 sec = 106.9 nm/sec.

This gave a maximum speed of 106.9 nm/sec. However, the speed measurements were limited by the frame recording frequency and should therefore be considered to be a minimum speed. The real growth rate is likely to be higher.

The same Cu growth was also achieved at a lower temperature but over a longer time period. For this experiment, BP was mechanically exfoliated onto a Cu grid and heated *ex situ* in a vacuum oven for 7 days at 110 °C (shown in **Fig.SI2)**. The Cu was found to diffuse through the BP flakes from the Cu grid, forming arrays of Cu heterostructures as shown in **Fig.SI2.b**. This shows that the process does not require heating to high temperatures in order to induce the diffusion of the Cu.

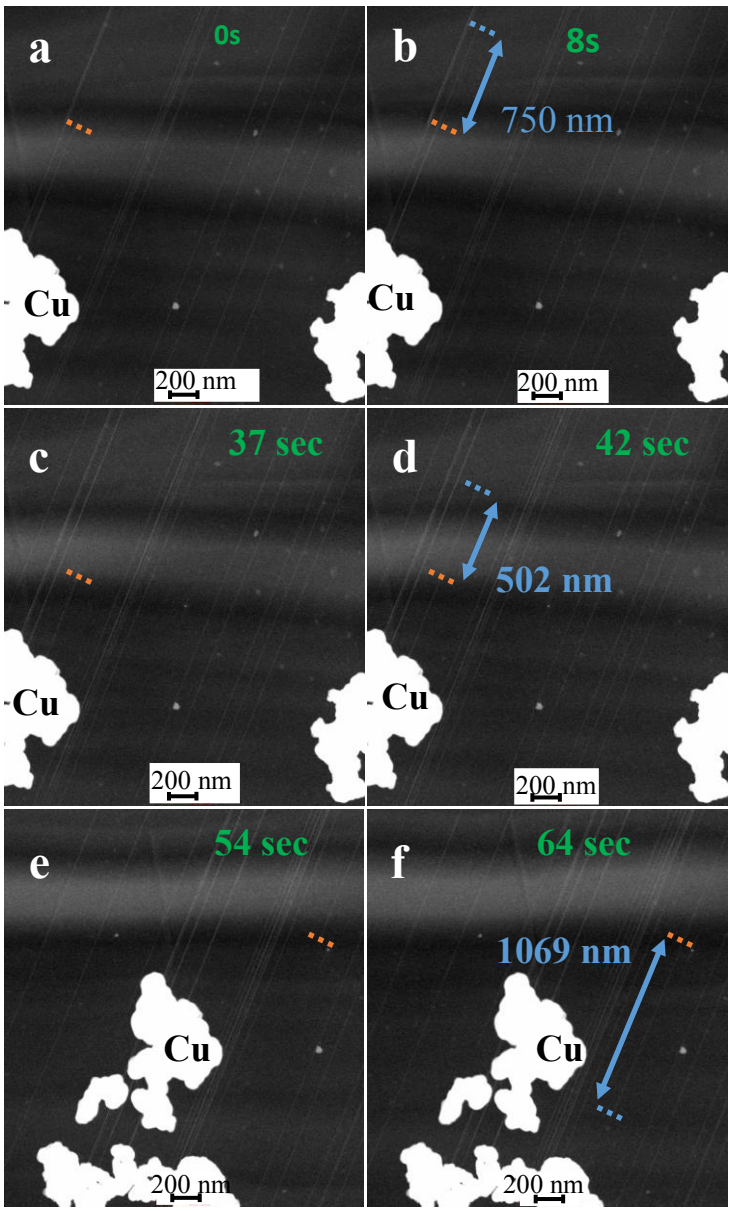

Fig.SI1: *Sequence of images from video (**V1**), showing Scanning Transmission (STEM) images, acquired at different time points:* ***a)*** *0s;* ***b)*** *8s;* ***c)*** *37s;* ***d)*** *42s;* ***e)*** *54s and* ***f)*** *64s. The white regions in the bottom part of the images show the Copper (Cu) nanoparticles from which the Cu heterostructure growth started. The images were acquired at different time points to calculate the speed of the formation of the arrays of Cu heterostructures. The orange dotted line represents the starting point from where the measurements were taken to the end point, the blue dotted line.*

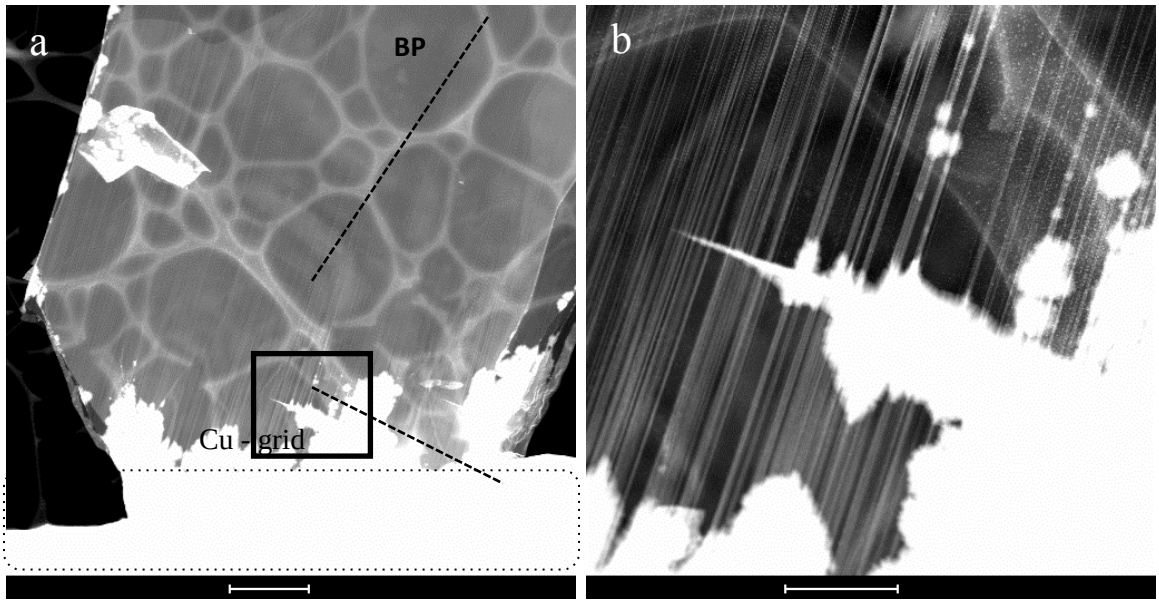

Fig.SI2: *Images of the ex-situ heating experiment wherein black phosphorous (BP) was heated for 7 days at 110 °C under vacuum on an electron microscopy (EM) Copper (Cu) grid to start the growth of Cu heterostructures in the BP at lower temperatures.* ***(a)*** *A lower magnification image (scale bar = 2µm) clearly shows the Cu from the grid after having migrated through the BP nanosheets, resulting in the formation of highly directional lines as shown in* ***(b)*** *(scale bar = 0.5µm).*

SI2 Orientations of Black Phosphorus

The **Fig.SI3** shows a schematic of the structure of a BP nanosheet, which helps to illustrate the Cu heterostructure growth direction. The R17 orientation gives the typical herringbone structure visible in the electron microscopy (EM) images of the R17 shown in the main paper as well as the SI. Aberration-corrected High-angle Annular Dark Field (HAADF) Scanning Transmission Electron Microscopy (STEM) imaging (discussed in the main paper) revealed that the Cu growth occurred along the zigzag (ZZ) direction only (orange arrow in **Fig.SI3**).

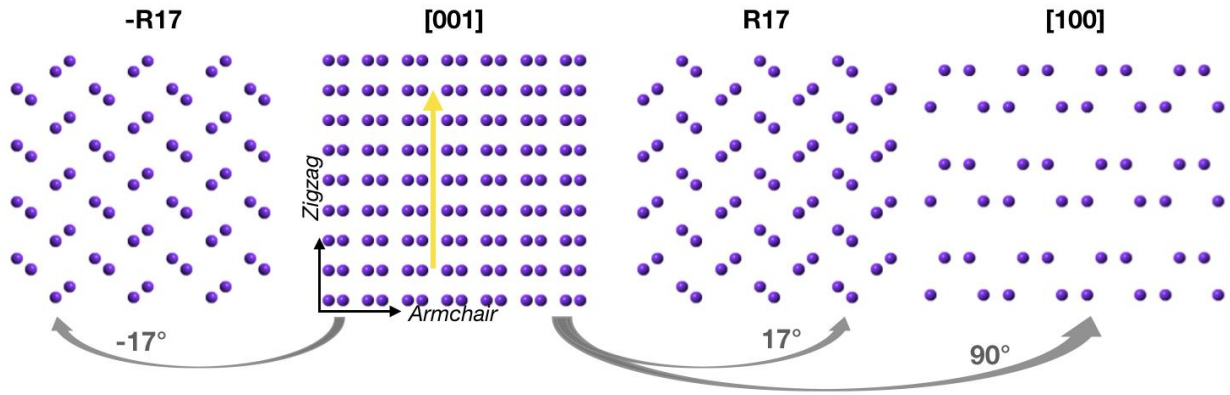

Fig.SI3: *Atomic model of a black phosphorus nanosheet viewed along the -R17, [001], R17 and [100]*

crystallographic directions respectively. The orange arrow in the [001] schematic shows the direction of the Cu heterostructure growth. The grey arrows indicate how many degrees of rotation are needed to obtain each projection. The [001], R17 and –R17 directions are visible in the transmission electron microscopy images shown in the main paper and the SI, the [100] direction however remained inaccessible due to the high angle of tilt needed to achieve this projection. Furthermore, R17 and –R17 are indistinguishable in the EM projections as they equivalent by symmetry.

SI3 Controlled instigation of self-assembly of Cu heterostructures

Technique1: Controlled instigation of Cu heterostructure growth by selective placement of seed-copper nanoparticles on BP sheets by the use of a micromechanical manipulator

Using a micromechanical manipulator controlled by a Kleindiek system, a fine needle (by Picoprobe) was used to place seed Cu nanoparticles on BP nanosheets (shown in **Fig.SI4(a**)). This was performed in a Carl Zeiss Auriga FIB system operated at 5kV. The Cu nanoparticles drop-cast on a silicon-wafer (Si-wafer) were lifted by Coulomb interaction between the nanoparticles and the needle (**Fig.SI4(b**)). They were then transferred onto a second Si-wafer where mechanically exfoliated BP had been deposited (**Fig.SI4(c**)). Next, the Si-wafer was heated to 300°C for 5min on a hot plate. The interaction between BP and Cu quickly became apparent as the Cu heterostructures appeared rapidly (white horizontal lines, marked with arrow in **Fig.SI4(d)**).

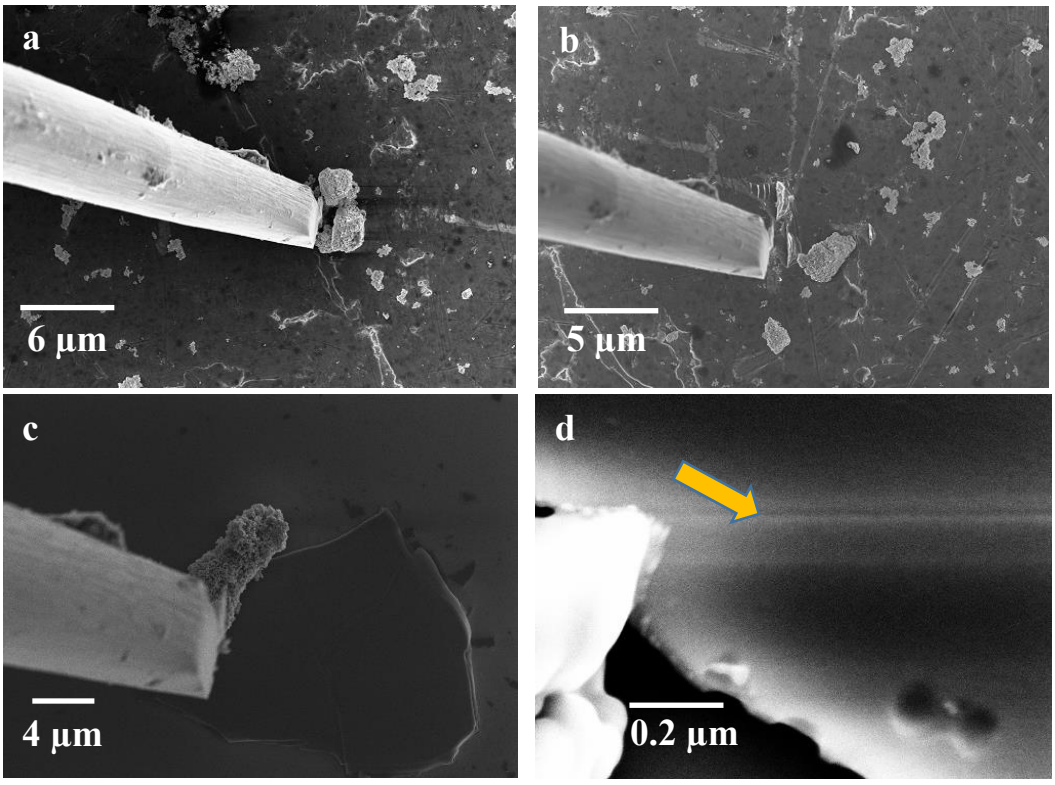

Fig.SI4: *Scanning electron microscopy (SEM) images showing technique 1 for controlled instigation of copper (Cu) growth by selective placement of seed copper (Cu) nanoparticles on black phosphorus (BP) nanosheets using a micromechanical manipulator needle in a dual-beam focussed ion beam instrument. Image* ***a)*** *shows the needle approaching the Cu nanoparticles drop-cast onto a SEM Aluminium stub. Image* ***b)*** *shows the successful lifting of the nanoparticles using the needle and* ***(c)*** *the subsequent dropping of the nanoparticles onto an exfoliated BP flake deposited on a silicon wafer. The aggregated nanoparticles on top of the BP nanosheets shown in* ***c)*** *were then positioned by the needle to enable the contact between a nanosized region of the BP nanosheet and the Cu nanoparticles as shown in* ***d).***

Technique 2: Controlled instigation of copper heterostructure growth by selective placement of seed copper on black phosphorus nanosheets through the use of e-beam lithography

In order to demonstrate the feasibility of growing Cu controllably on certain BP nanosheets only, we used e-beam lithography (EBL) to selectively deposit seed Cu on the nanosheets. This method consisted of transferring the exfoliating BP nanosheets onto a Si-wafer, followed by lithography and deposition of Cu by e-beam metal evaporation and thermal heating.

The diffusion of Cu only took place in the region where the Cu was deposited. The Si wafer was heated on a hot plate to 300°C for 3min and was imaged by Scanning Electron Microscopy (SEM) as shown in **Fig.SI5(a)**. The yellow rectangle marked in **Fig.SI5(a)** shows a 60nm Cu aggregate deposited (Temescal)

by EBL (E-beam Lithography) on a BP nanosheet. SEM imaging confirmed that the growth of the Cu heterostructures occurred only in the selected regions (**Fig.SI5(b)**), whereas no Cu was found in neighbouring regions (**Fig.SI5(c)** depending on the orientation of the BP nanosheet. No Cu was observed to migrate in the direction perpendicular to the growth of the heterostructures. This further supports the conclusion that the Cu growth occurs in grooves of the BP lattice along the [010] direction. As an additional benefit of having elucidated this anisotropic growth mechanism of the Cu heterostructure, this allows us to identify the orientation of the BP nanosheet simply by looking at the Cu heterostructure direction in the SEM (directions marked as AC (Armchair) and ZZ (Zigzag) in **Fig.SI5(d)**).

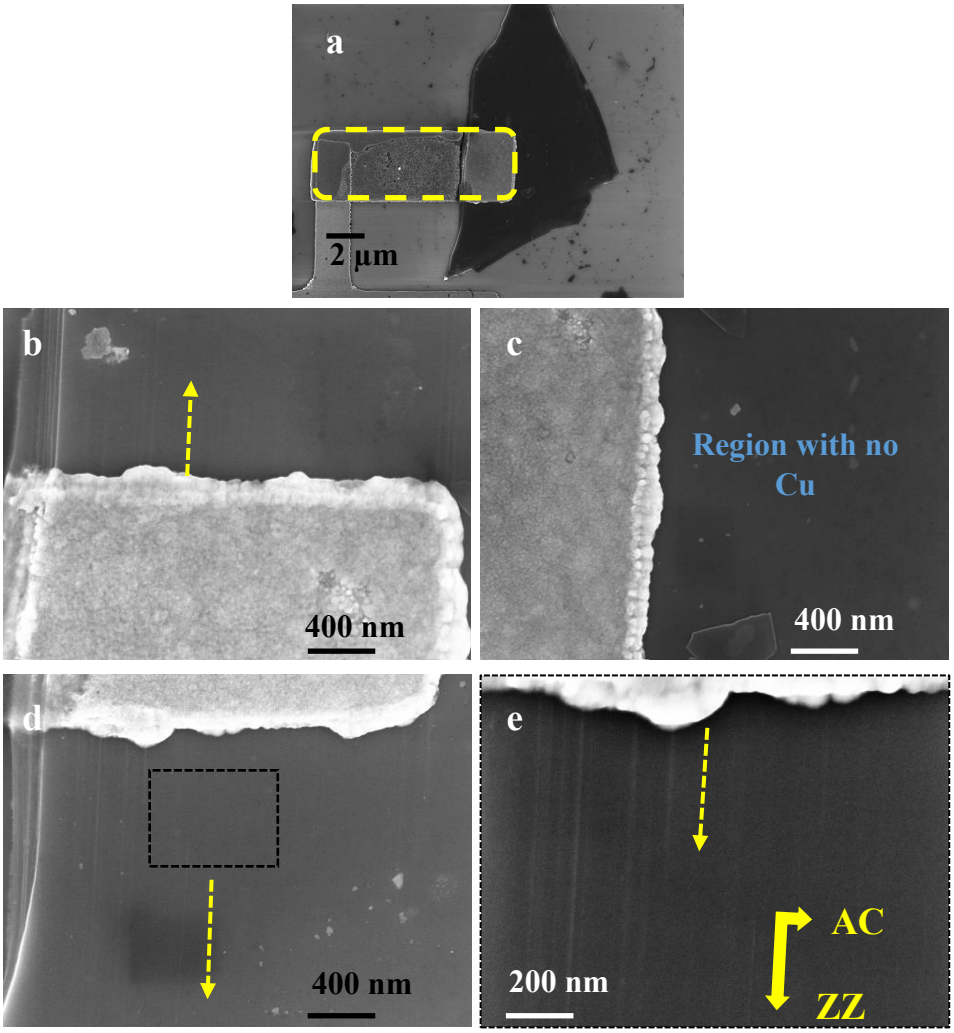

Fig.SI5: *Scanning Electron Microscopy (SEM) images showing technique 2 for controlled instigation of copper (Cu) heterostructure growth by selective placement of seed copper (Cu) on black phosphorus (BP) nanosheets by the use of e-beam lithography (in-lens detector) carried out on a BP nanosheet. Image* ***a)*** *shows an overview of a 60nm sized Cu (marked in yellow) deposit on top of BP nanosheets. Cu*

*heterostructures were formed in some regions as shown in **b)** and not in neighbouring regions as shown in **c)**. In region **b)** above the Cu, the BP lattice is in the correct position for the Cu arrays to form whereas region shown in **c)** is not. This further supports the conclusion that the Cu growth occurs in grooves of the BP lattice along the [010] direction and never in any other direction.*

SI4 Undulations of copper heterostructures and spacing between copper heterostructures in black phosphorus

The undulations as well as the spacing between individual Cu heterostructures as shown in the High Angle Annular Dark Field (HAADF) Scanning Transmission Electron Microscopy (STEM) images in **Fig.SI6 (a&b)** were both found to be regular. The undulations were consistently found to be 2nm in periodicity in the [001] orientation as shown in **Fig.SI6(c)**. The spacing between the heterostructures was found to follow a trend of multiples of the calculated distances of 0.451nm between grooves in the BP lattice as shown in the schematic in **Fig.SI6 (d**). The measured values follow the trend of the calculated values closely as shown in **Fig.SI6 (e**), blue points and orange dotted line respectively.

Additional images of the heterostructures are shown in **Fig.SI7 and Fig.SI8.**

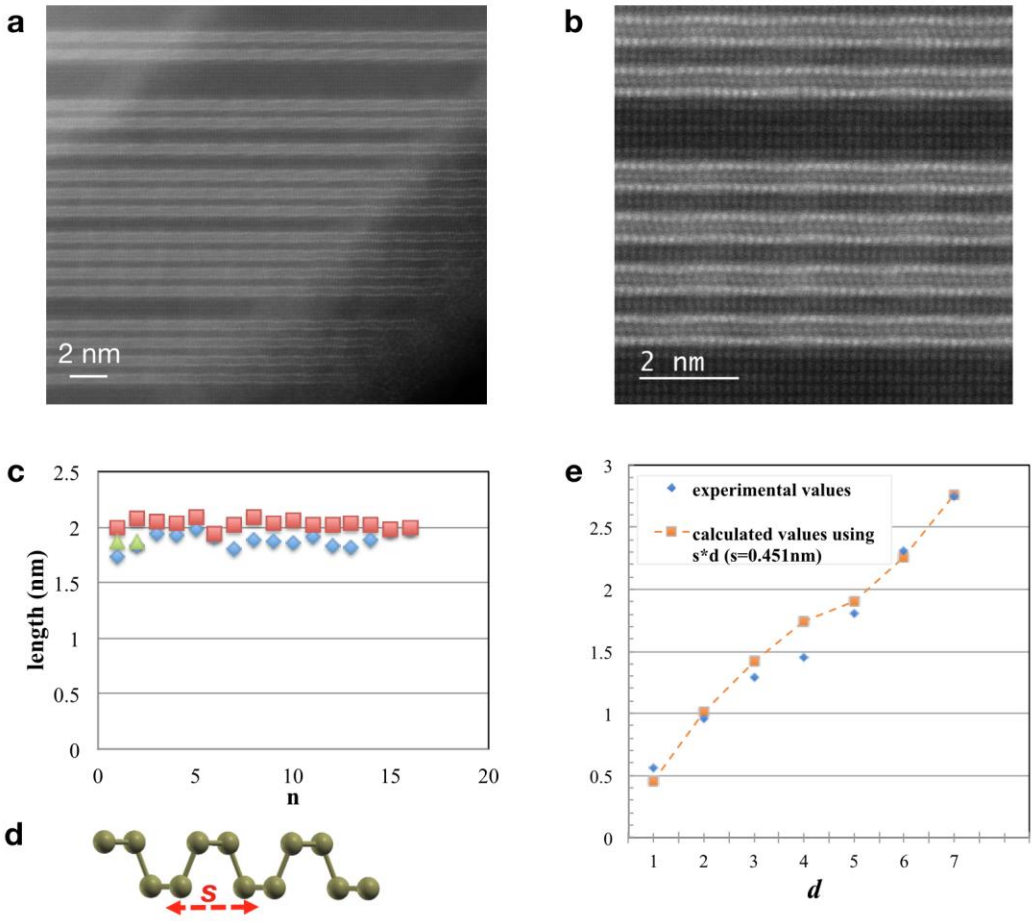

Fig.SI6: *The undulations of the heterostructures and the separation of copper (Cu) heterostructures as formed in the BP nanosheets are shown in the High Angle Annular Dark Field (HAADF) Scanning Transmission Electron Microscopy (STEM) images in* ***a)*** *and at high magnification in* ***b).*** *Both were found to be regular.* ***c)*** *The undulations were 2nm in length in the [001] orientation. These were calculated per Cu heterostructure (n = number of undulations measured per heterostructure). And the separations between the heterostructures were found to be multiples of the calculated distances 's' as shown in the schematic in* ***d)****.* ***e)*** *The values measured in the STEM images (blue data points) followed the trend (orange line) of calculated values of multiples of the theoretically calculated distances of s=0.451nm.*

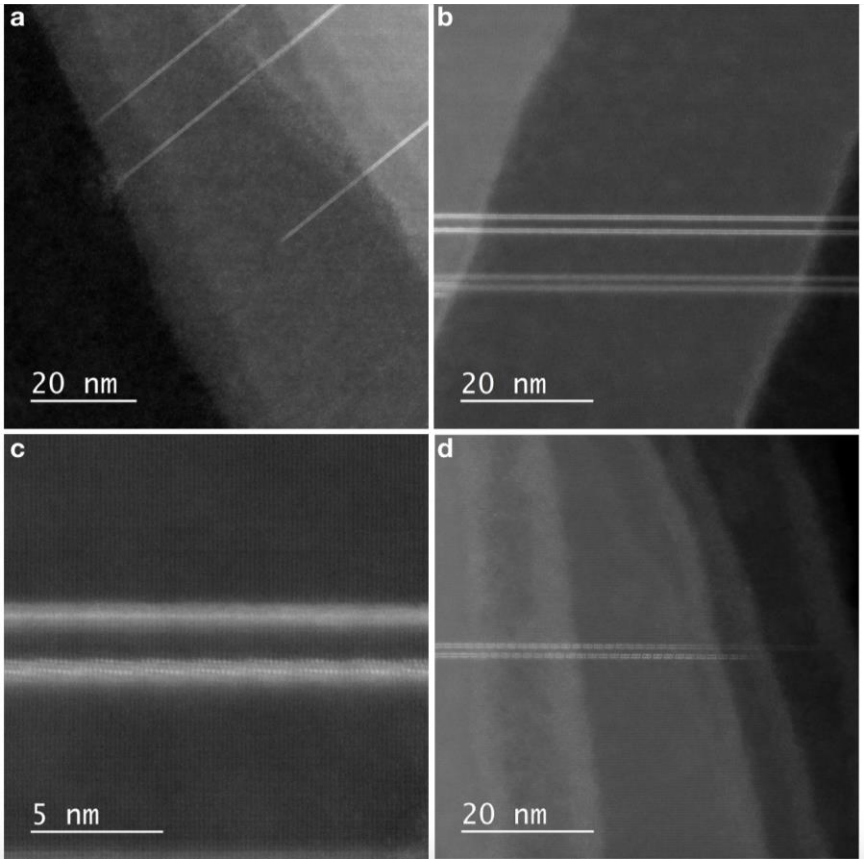

Fig.SI7 *Additional High-resolution High-angle Annular Dark Field (HAADF) Scanning Transmission Electron Microscopy (STEM) imaging of copper (Cu) heterostructures in black phosphorus (BP) nanosheets. Image* ***a)*** *shows a Cu heterostructure that appears to terminate in the BP sheet. Image* ***b)*** *shows two pairs of heterostructures of very different intensities in the same region of a BP nanosheet.* ***c)*** *The Cu heterostructures exhibit variations in the undulating patterns at a 5° tilt away from the zone axis. The undulating pattern was found to vary across the structures: here, the top structure appears straight and the bottom structure exhibits clear undulations. This was observed in regions of similar BP thickness. Image* ***d)*** *shows a pair of heterostructures of very different intensities in the thinner regions of the BP nanosheet.*

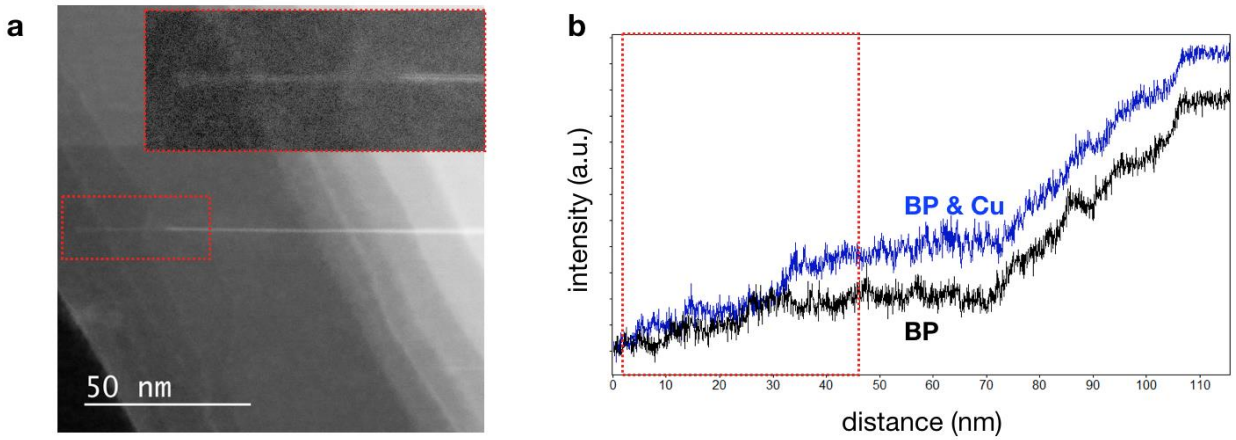

Fig.SI8: Example of individual copper structure in BP nanosheet displaying varied intensity along the length of the structure and finally terminating in the BP nanosheet away from the BP edge. ***a)*** *HAADF STEM imaging acquired at 10° tilt from the zone axis for more accurate intensity measurements and* ***b)*** *corresponding line profile for the Cu and the BP nanosheet. The Cu intensity the HAADF STEM images changes in intensity compared to the BP nanosheet intensity (marked with the red dotted line in the images and the line profile).*

SI 5 Computational Approach and Modelling

The density functional theory (DFT) approach was applied as implemented in the CP2K suite of codes (www.cp2k.org). Kohn and Sham orbitals were expanded in a mixed Gaussian (double-ζ plus polarization, DZVP) and plane-waves basis set. A 600 Ryd energy cut-off was used for the plane-wave expansion of the electronic density. Tether and Goedecker-type pseudopotentials were used for all atoms, and BZ integration was restricted to the Γ-point. The geometry and cell of each system were relaxed until the maximum force on each atom was less than 0.01 eV/Å. PBE [1] exchange and correlation functionals with a Van der Waals correction at the Grimme-D3 level [2] were used.

Bulk BP is modelled using a monoclinic cell with a=26.814 Å, b=33.149 Å, c=16.581 Å, α=73˚, β=90˚ and γ=90˚. The BP surface slab is obtained by replicating in plane 6 x 10 times the unit surface cell for BP. The repetition unit along z is represented by a three layers BP slab (the cell equilibrium parameters obtained for this BP bulk model are a = 3.31 Å, b = 4.48 Å and c=5.28 Å).

We assessed that our cell size was sufficiently large to provide a good representation of the surface Brillouin zone (BZ) at Γ, verifying that the total energy of the BP system calculated with the ESPRESSO code (www.quantum-espresso.org) - using the unit cell and sampling the Brillouin zone (BZ) with a Monkorst & Pack k-points grid - converged for an in plane BZ sampling density corresponding to that

used in our calculations. The error in the evaluation of total energy per P atom and lattice parameter using a BP bilayer as repetition unit along z amounts to < 0.01 eV and <0.2 Å, respectively.

Interstitial periodical 2D heterostructures within BP are modelled by inserting Cu atoms within the relaxed bulk structure and subsequently relaxing again geometry and cell parameters. These 2D heterostructures are obtained by periodically repeating along z (every 2 or 3 BP layers) interstitial 1D nanowires. The geometry, electronic structure and formation energy of different heterostructures are studied.

Adsorption energies per Cu atom were evaluated as $\Delta E = (E_{BP}+nE_{Cu}-E_{CuADSORBED}-n'E_P)/n$, where E_{BP} is the energy of the reference bulk BP slab, E_{Cu} is the energy of a Cu atom (taken from a reservoir represented by a 841 atoms Cu cluster), $E_{CuADSORBED}$ is the energy of the *decorated* BP slab, *n* is the number of the adsorbed Cu atoms (NCu in the table in next paragraph) and *n'* the number of P atoms that have been released (Psubst in the table in next paragraph). E_P is the energy of a P atom, taken from a reservoir represented by the ideal BP reference. To minimise the error on the evaluation of the heterostructure formation energy, either the energy of a BP bulk slab obtained replicating along z a BP trilayer or that obtained replicating a BP bilayer unit is used as a reference (depending on the heterostructure periodicity along z).

To model clean and Cu-decorated BP monolayers (namely, a phosphorene layer), and study Cu adsorption on BP surface a supercell with 240 P atoms was used, obtained by replicating 6 x 10 times the orthogonal unit surface cell for BP. Different images of the monolayer along z are separated by a vacuum region of approximately 20 Å.

To study structure and formation energy of BP edges we simulated two slightly smaller phosphorene nanoribbons (PN) (see **fig.SI9**). The PN models for each edge are obtained by replicating the phosphorene unit surface cell 9 x 6 times along (100) and (010) directions, respectively. These PN are periodic along one direction and are truncated perpendicularly to the edge under consideration. A vacuum region 20 Å wide separates the periodically repeated replica of the nanoribbon along this direction. The edge formation energy along the [100] and [010] directions (zigzag and armchair edges, respectively) amounts to ΔE = 318 mJ/m^2 and ΔE = 293 mJ/m^2, respectively. The edge formation energy is evaluated by looking at the difference between the energies of the nanoribbon and that of the ideal phosphorene nanoflake, renormalized to the number of P atoms composing the nanoribbon

$$\Delta E \quad = lim_{n\to\infty} \frac{1}{2}(E^n{}_{ribbon} - n * E_{mono}),$$

where E^n_{ribbon} was the total energy of a nanoribbon composed of *n* atoms, and E_{mono} was the energy per atom of an ideally periodical phosphorene layer.

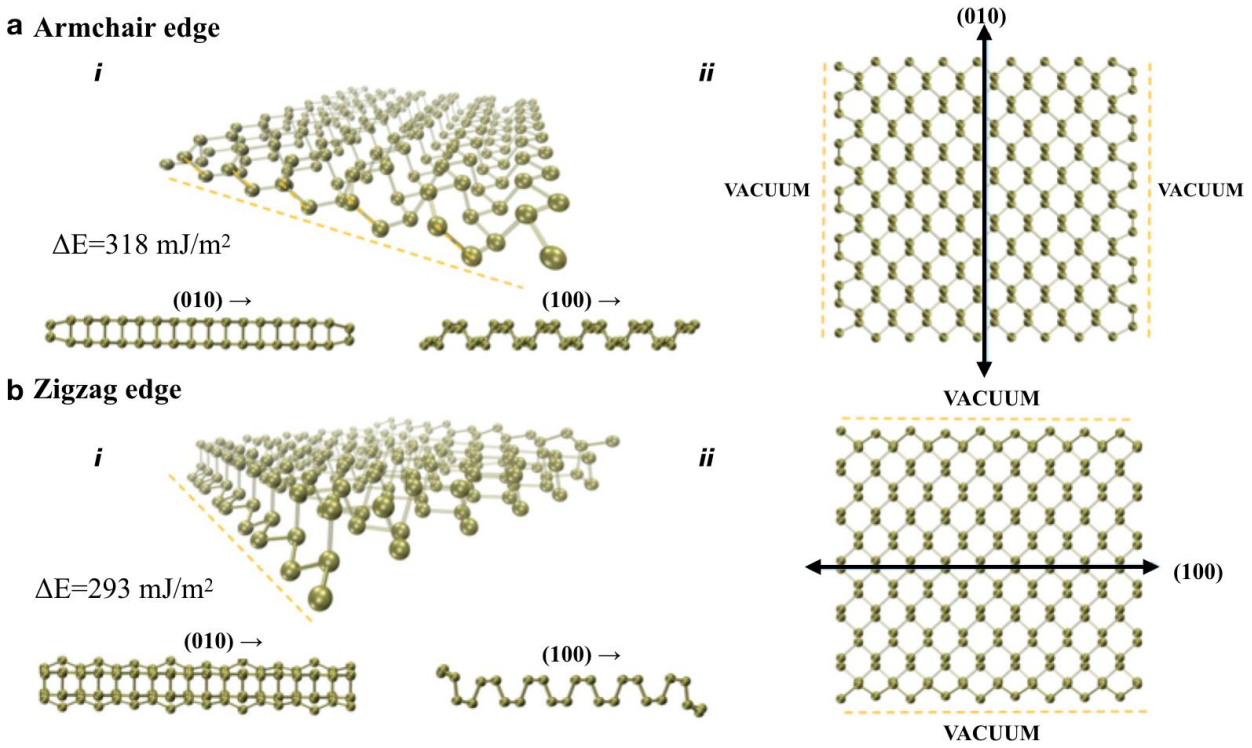

Fig. SI9: Schematics of the Black Phosphorus (BP) nanoribbon structure and formation energy of the edges as used in the simulations. *Edge structures and formation energy of* ***a)*** *armchair and* ***b)*** *zigzag edge are shown here.* ***i)*** *3D representation of the two nanoribbons as studied, as well as their side view and formation energy.* ***ii)*** *Top view of the simulated nanoribbons. The arrowed black lines indicate that the nanoribbon is periodical along that direction. Green balls represent P atoms. Orange dashed lines signal the edges.*

The investigation of the energetics of the Cu diffusion process in BP nanosheets found the most stable structure of one interstitial Cu atom on BP surface to be as shown in **fig.SI10(a,i-ii)**. The Cu diffusion pathway was found to occur by adsorption at consecutive sites following a zigzag route as shown in **fig.SI10(b)**. The activation barrier for the Cu diffusion into the BP sheet was found to be 0.14eV/atom for Cu diffusion through BP lattice (**fig.SI10(c)**). When comparing adsorption energy versus heterostructure length it was found that the Cu adsorption on a BP surface is initially endothermic but becomes progressively more favourable when the structure becomes longer (**fig.SI11)**. This increase in favourability of the process helps in explaining the fast speed of formation of the heterostructures observed *in situ*.

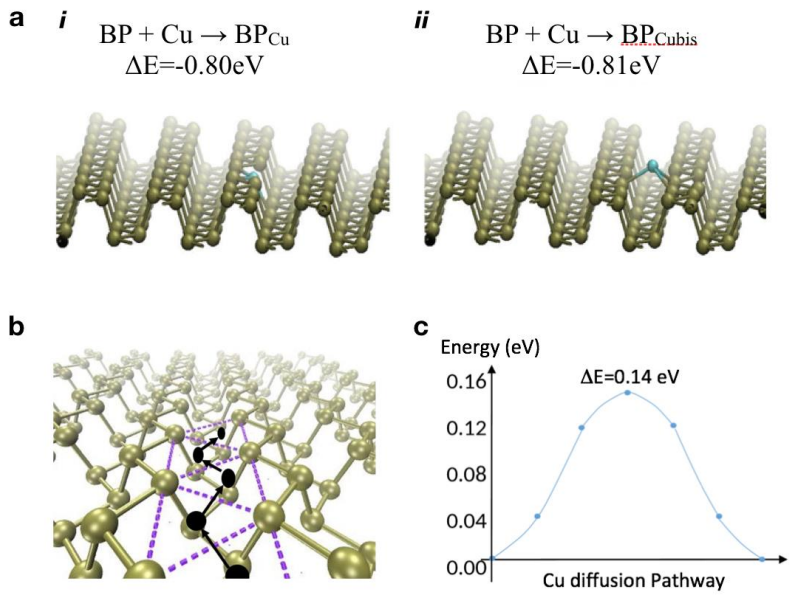

Fig.SI10 Computational investigation of the energetics of Copper (Cu) adsorption on the Black Phosphorus (BP) nanosheets. a) *Adsorption of a Cu atom on the surface of a phosphorene layer is endothermic and the sites for Cu adsorption are shown in* ***i)*** *and* ***ii)***. ***b)*** *Cu diffusion pathway occurring by adsorption at consecutive sites following a zigzag route (adsorption sites are highlighted in black were always found at the centres of the triangles, annotated in purple).* ***c)*** *The activation barrier for the Cu diffusion into the BP sheet was found to be 0.14eV/atom for Cu diffusion through BP lattice.*

The formation of the 2D heterostructure is further stabilised by growing interstitially within BP layers and by the interaction between wires in different layers.

The dissociative adsorption of an isolated Cu atom at the 101 edge as shown in **fig.SI13** was found to be exothermic by 0.02 eV and close to the edge endothermic by 0.2 eV is more energetically favourable than its adsorption in the middle of the surface which was found to be endothermic by 0.84 eV. The structure as observed experimentally is therefore expected to start at the edges of stepped surfaces or at defect sites, such as vacancies possibly present on BP surfaces.

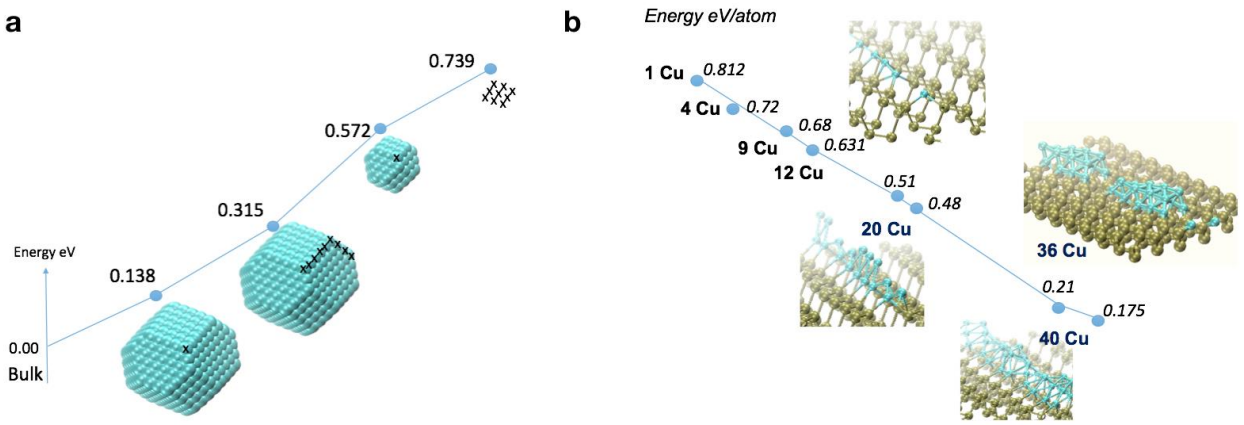

Fig.SI11: Computational investigation of the energetics of the copper (Cu) structure formation process in black phosphorus (BP) nanosheets. a) *The cost for extracting Cu from its reservoir.* ***b)*** *Adsorption energy vs. Cu structure length: Cu adsorption on a BP surface is initially endothermic but becomes progressively more favourable when the structure becomes longer.*

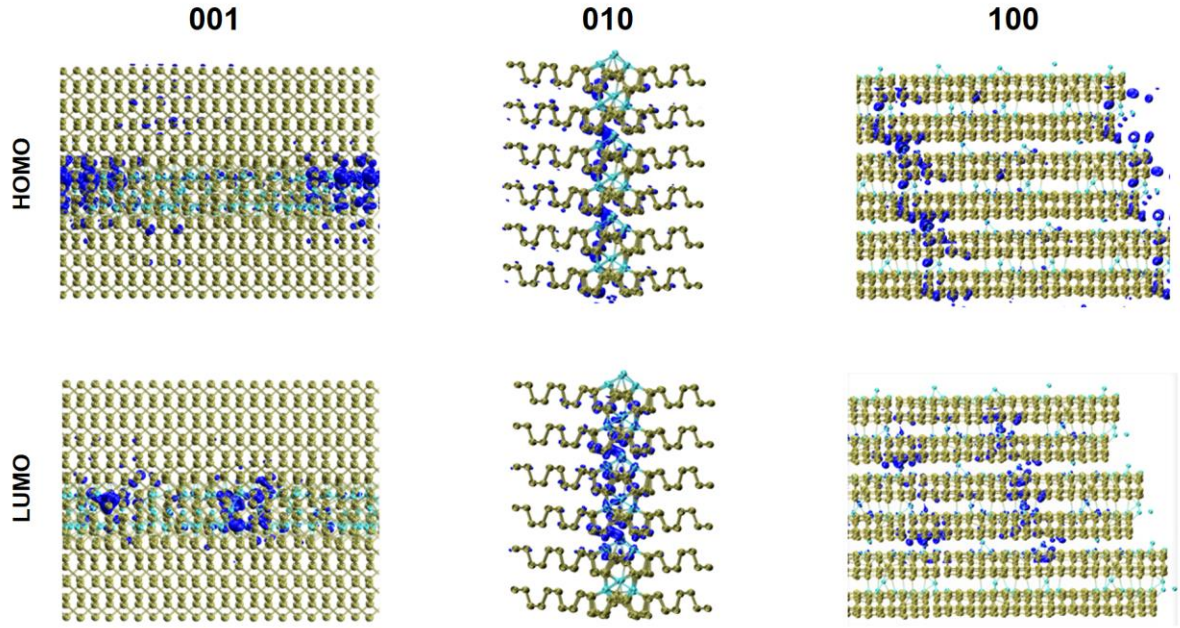

Fig.SI12: Isosurfaces (+0.014 |e| and -0.014 |e| both in blue) of the molecular orbitals for the system T-S-3 corresponding to Fermi energy level (HOMO top row) and the first level immediately above it (LUMO bottom row). *001, 010 and 100 orientations are shown from left to right, respectively and show*

localization of the states around Fermi level around the wire. Green and cyan balls represent P and Cu atoms respectively.

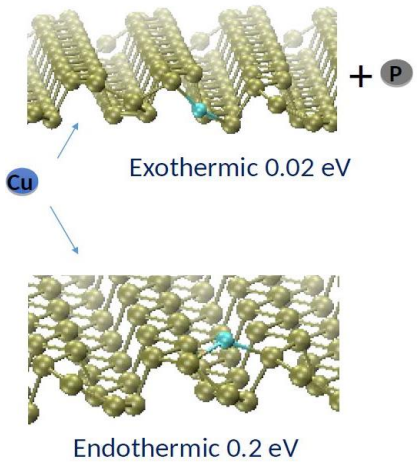

Fig.SI13 *The dissociative adsorption of an isolated Cu atom at the 101 edge (exothermic by 0.02 eV) and close to it (endothermic by 0.2 eV) is more favorable than its adsorption in the middle of the surface (endothermic by 0.84 eV). The growth of the 2D heterostructure is therefore expected to start at the edges of stepped surfaces or at defect sites, such as vacancies possibly present on BP surfaces.*

SI 6 DFT possible structures catalogue

Using the computational methods outlined in section **SI5** and the main manuscript, a number of energetically favourable and stable structures were found. The most closely matched structure is described in the main manuscript.

Every intercalated triangular wire composing the 2D heterostructure has a periodic structure with the shape of a parallelogram, which repeats every 5 BP lattice parameter lengths along [010] direction. The long sides of the parallelogram contain 4 Cu atoms whilst an angle of ~70˚ is formed between the short side of the parallelogram and [010] direction. A missing Cu atom separates periodically repeated structures. Notably the computational relaxation of the structure into the 4(3)-1(2) dinghy motifs for Cu atoms was spontaneous and not biased by the adopted cell symmetry, which can accommodate a multiple of the experimentally observed repetition unit. A slight local compression (<1%) along the [010] direction and expansion along the [100] direction is expected, reflecting the small difference in the relaxed cells of clean and decorated BP system.

The most closely matched DFT structure is shown in **Fig.SI14** in 001 and **Fig.SI15** in R17/-R17 orientations. Here we replicated the repetition unit for the structure (our supercell) (1 time replicated in the x direction, 2 times replicated in y and 3 times replicated in z) to generate longer heterostructures as seen in the [001] orientation in the electron microscope. The simulated image **Fig.SI14(b**) shows the same undulations of the structure in this orientation as observed experimentally and shown in **Fig.SI14(c**). The chiral DFT structure also introduces a step into the BP lattice when observed in the –

R17 orientation, visible in the simulated images shown in **Fig.SI15(b**) but not the R17 orientation. These findings confirm that the chiral nature of the heterostructure is at the origin of these variations observed experimentally.

In addition to the good qualitative visual match between the image contrast in the experimental and those simulated from the DFT structure, we also found that the Cu-Cu interatomic distances in the external sides of the three atom thick structure ranged between 0.26 and 0.39 nm; the inter-wire distance was about 0.56 ± 0.007 nm in the [001] direction, and the overall average width of the Cu heterostructure was 0.369 ± 0.004nm, which is within the error margin of the experimental value of ~0.37 ± 0.015 nm (main text, **fig.2**).

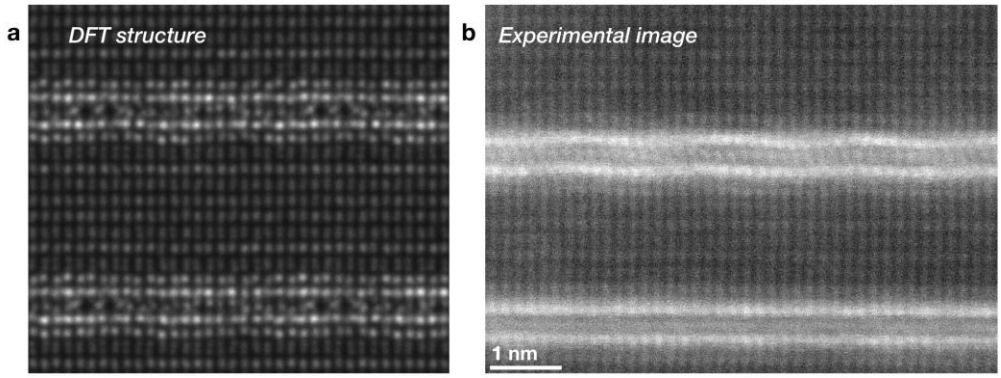

Fig.SI14 Simulated images of the replicated structure (123) of the copper (Cu) heterostructures in black phosphorus (BP) nanosheets that best matched experiment were compared to experimental electron microscopy images in [001] orientation. a*) &* ***b)*** *Simulated image showing the replicated structure (123) that was found to provide the closest match with experiment in orientation [001]* ***c)*** *Experimental image showing the same orientation for comparison. The simulated image b) shows the undulations of the structure in this orientation as observed experimentally and shown in c).*

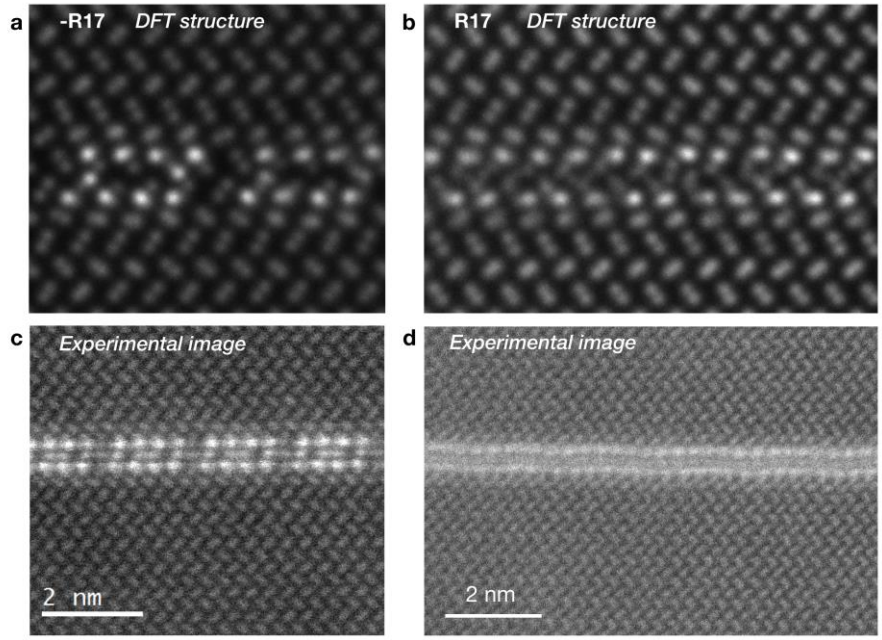

Fig.SI15 Simulated images of the structure (123 repetition units) of the DFT copper (Cu) heterostructures in black phosphorus (BP) nanosheets that best matched experiment were compared to experimental electron microscopy images in orientation a) R17 and b) -R17. *The experimental images of the structure in the R17/-R17 orientations are shown for comparison: the regular gap is visible in some regions as shown in* ***c)*** *but not visible in others as shown in* ***d)****. The simulated image in* ***a)*** *shows that the DFT structure displays the regular gap in the –R17 but not the R17 orientation. The chiral DFT heterostructure also introduces a step visible in the EM projections into the BP lattice in the –R17 but not the R17 orientation. This finding explains the same observation in the experimental EM images.*

Aside from the best matched 2D heterostructure, we also compiled a catalogue of the 2D heterostructures that were found to be energetically favourable as they are likely to also exist experimentally. A selection of these structures and their corresponding energies is shown in **table SI.T1**. In addition, images of these structures were also simulated using the Prismatic STEM image simulation tool [3] to compare to the experimentally observed heterostructures and these images are shown in R17 and [001] orientations in **table SI.T1.**

Table SI.T1 (provided in separate file): ***Catalogue showing the stable and energetically favourable 2D copper (Cu) heterostructures within black phosphorus (BP) bulk as found using an iterative combination of density functional theory (DFT) and image simulation* (*Prismatic).*** *Column* ***a)*** *gives the system name, structure cross-section of Black Phosphorus, energy per Copper (Cu) atom (Ene/Cu (eV)), energy per surface (Ene/Surf (eV/nm^2)), number of Cu atoms (NCu), number of Phosphorus (P) atoms*

(NP), number of P atoms released in the adsorption process (Psubst), whose sites are now occupied by Cu atoms. Geometry and cell of all systems have been relaxed until forces on each atom are smaller than 0.01 eV. The relaxed cell dimensions are given in ***a)****.* ***b)*** *The ball and stick representation of 001 and R17/-R17 surfaces are shown as well as the* ***c)*** *ball and stick representation of 010 and 100 surfaces.* ***d)&*** ***e)*** *Simulated images of the DFT structure in 001 and R17orientations respectively (or –R17, chosen depending on structure as the orientation displaying the regular gaps was chosen here for simplicity) were obtained using image simulation software Prismatic and the source size was added (details of the methodology and exact settings are described in the main paper in the 'methods' section). The structures were image simulated using 113 repetition units unless stated otherwise.* ***f)*** *Density of States (DOS) of the clean reference system (BP bulk – obtained replicating along z either a BP bilayer or a trilayer) as well as the total DOS for the decorated system and their projection on Cu and P centred states are shown here.*

References:

1. Perdew, J.P., K. Burke, and M. Ernzerhof, *Generalized gradient approximation made simple.* Physical Review Letters, 1996. **77**(18): p. 3865-3868.
2. Grimme, S., et al., *A consistent and accurate ab initio parametrization of density functional dispersion correction (DFT-D) for the 94 elements H-Pu.* J Chem Phys, 2010. **132**(15): p. 154104.
3. Ophus, C., *A fast image simulation algorithm for scanning transmission electron microscopy.* Adv Struct Chem Imaging, 2017. **3**(1): p. 13.

Table SI.T1: Catalogue showing the stable and energetically favourable 2D copper (Cu) heterostructures within black phosphorus (BP) bulk as found using an iterative combination of density functional theory (DFT) and image simulation (Prismatic).

<table>
<tr><td rowspan="2">a) Name, System cross-section Ene/Cu (eV) Ene/Surf (eV/nm^2) N_{Cu}, N_P, P_{subst} CELL (Names reflect the symmetry of the unit wire cross-section, that can be Triangular (T), Pentagonal (P) and Hexagonal (H). S indicates that the structure as the opposite chirality.)</td><td rowspan="2">b) Ball and stick planes 001, R17, -R17</td><td rowspan="2">c) Ball and stick planes 010 and 100</td><td>d) Simulated image in 001</td><td>e) Simulated image in R17 / – R17</td></tr>
<tr><td colspan="2">f) Density of States (DOS) of the clean BP bulk (shaded light green area), Total DOS for the decorated system (black) and its projection on Cu (green) and P (red) centred states</td></tr>
</table>

T-1

Triangular (T)
Formation energy
0.70/3.15
NCu= 40
Nphos= 480
Psubst= 0
Relaxed cell
27.167
32/881
11.552

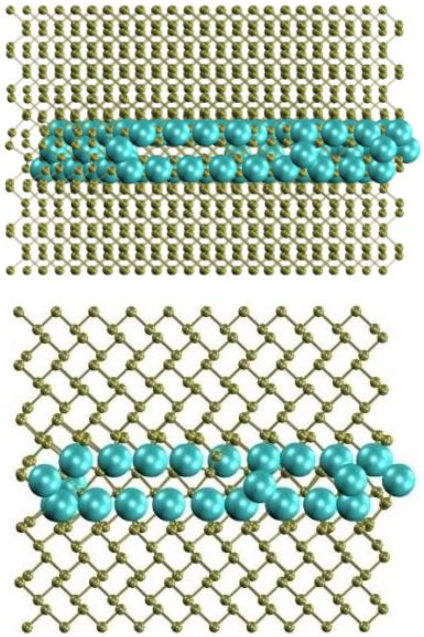

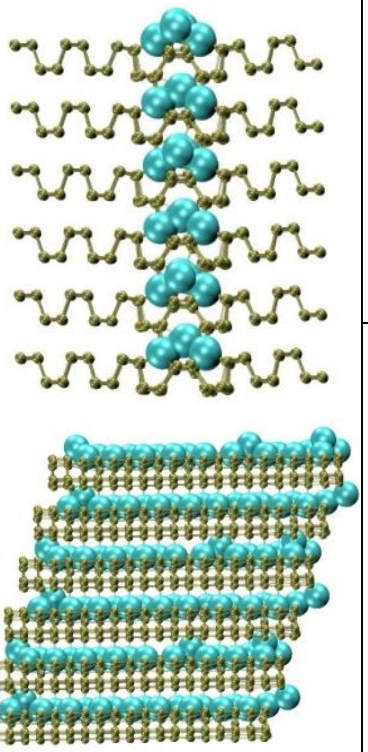

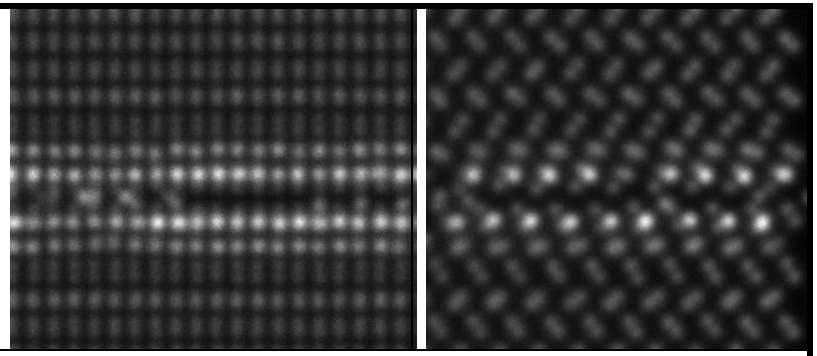

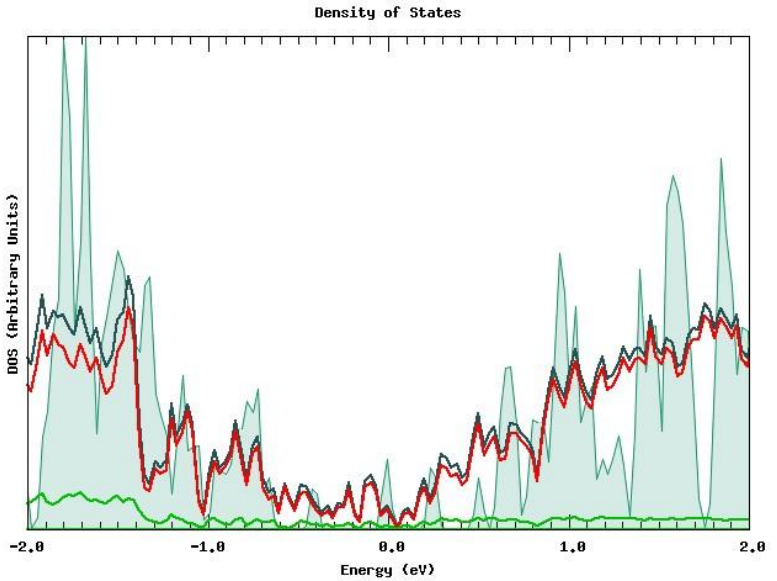

T-2

Triangular (T)
Formation energy
0.66/3.25
Interstitial
NCu= 44
Nphos= 480
Psubst= 0
Relaxed cell
27.114
32.926
11.615

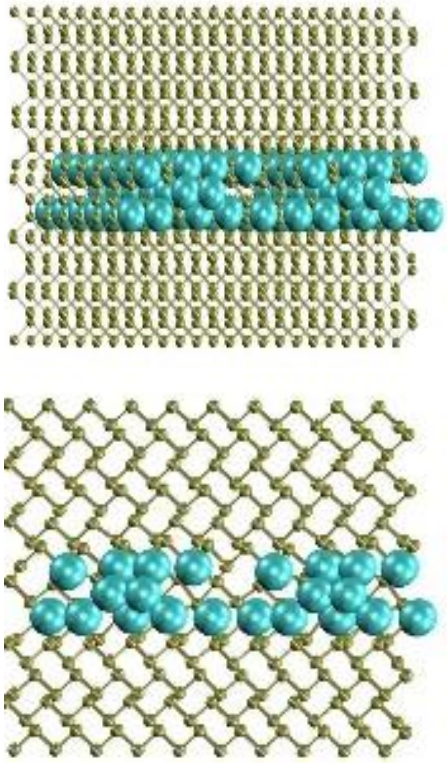

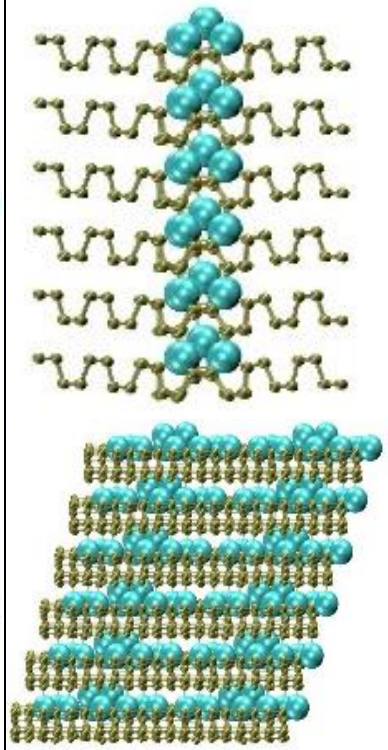

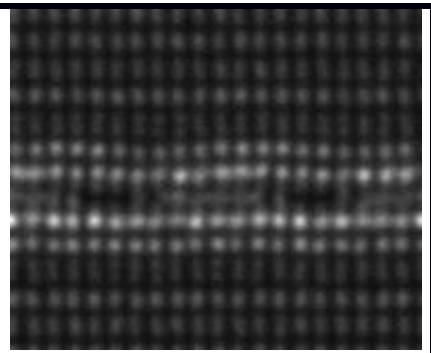

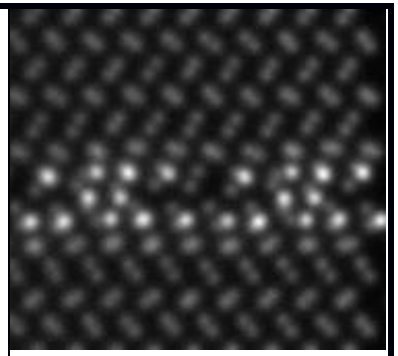

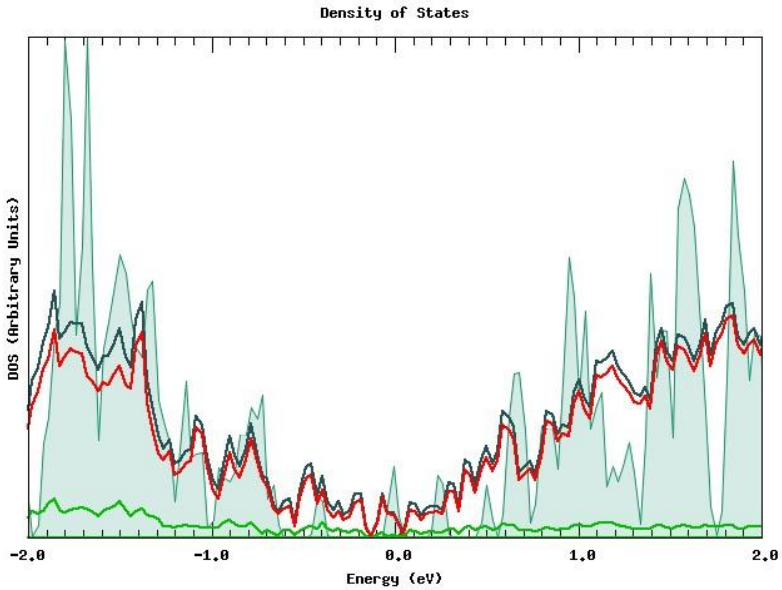

T-3

Triangular (T)
Energy
0.64/2.87
NCu= 40
Nphos= 480
Psubst= 0
Relaxed cell
(Running)
27.162
32.889
11.593

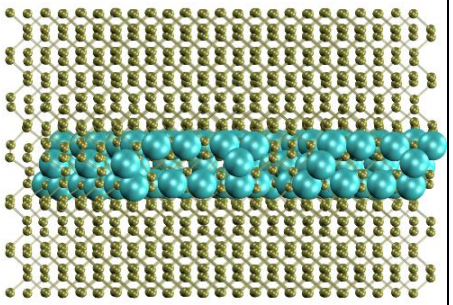

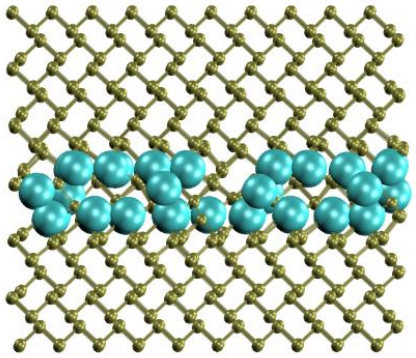

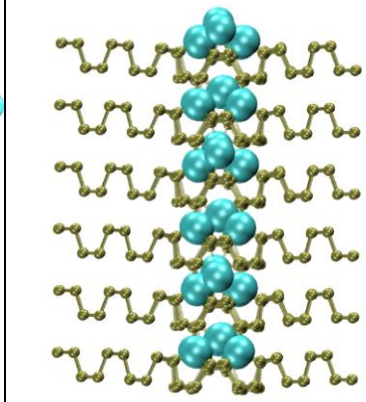

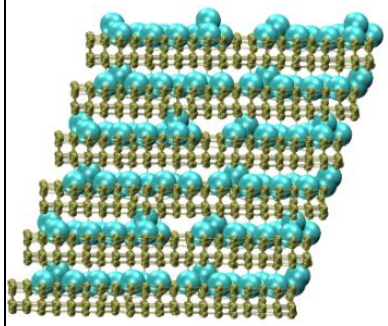

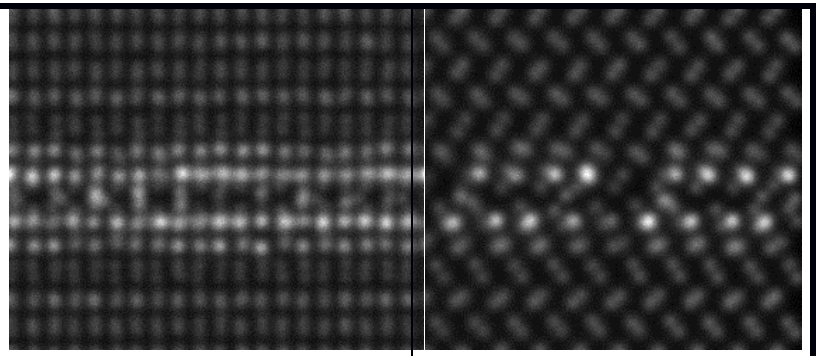

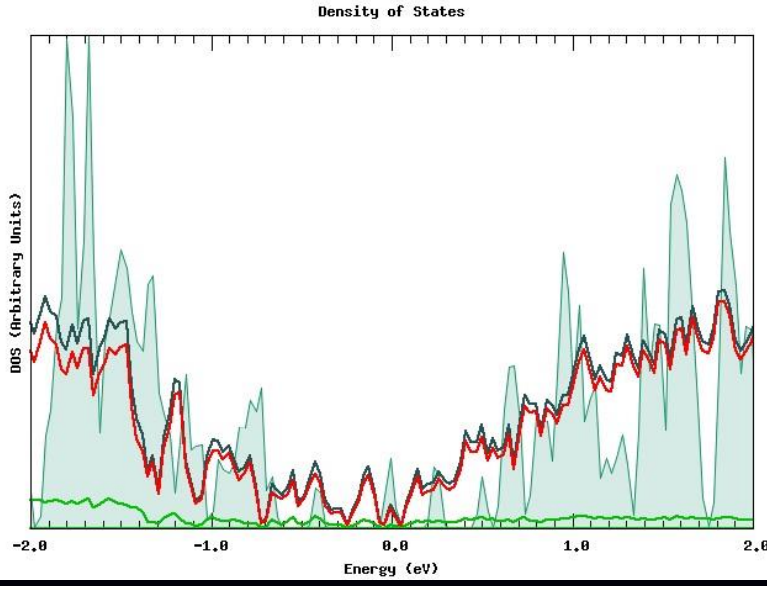

T-4

Triangular
Energy
0.64/2.78
NCu= 39
Nphos= 480
Psubst= 0
Relaxed cell
27.167
32.900
11.606

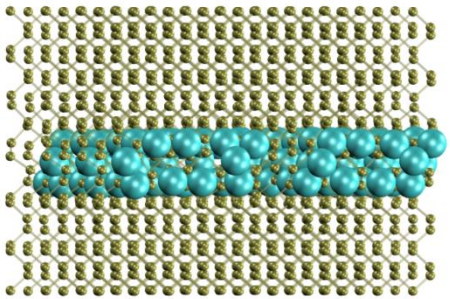

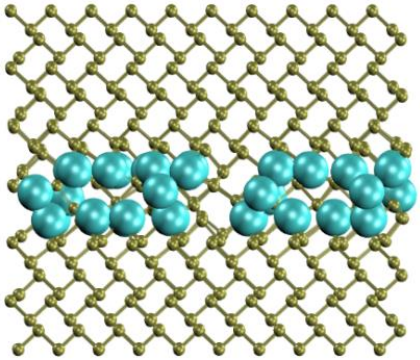

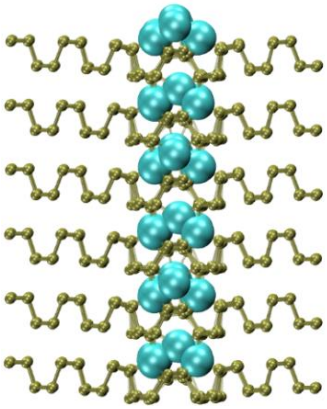

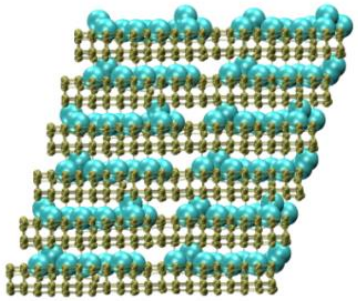

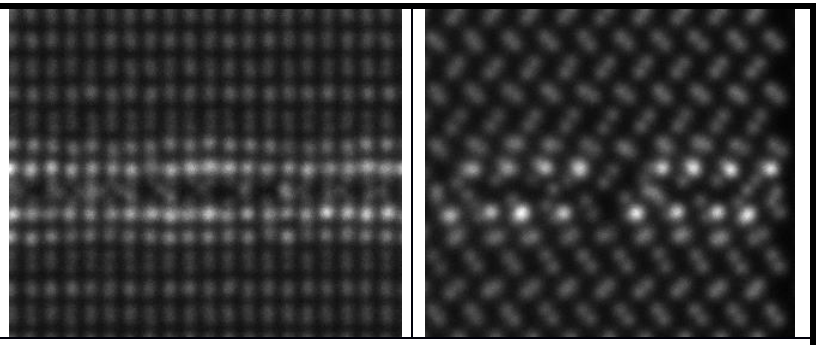

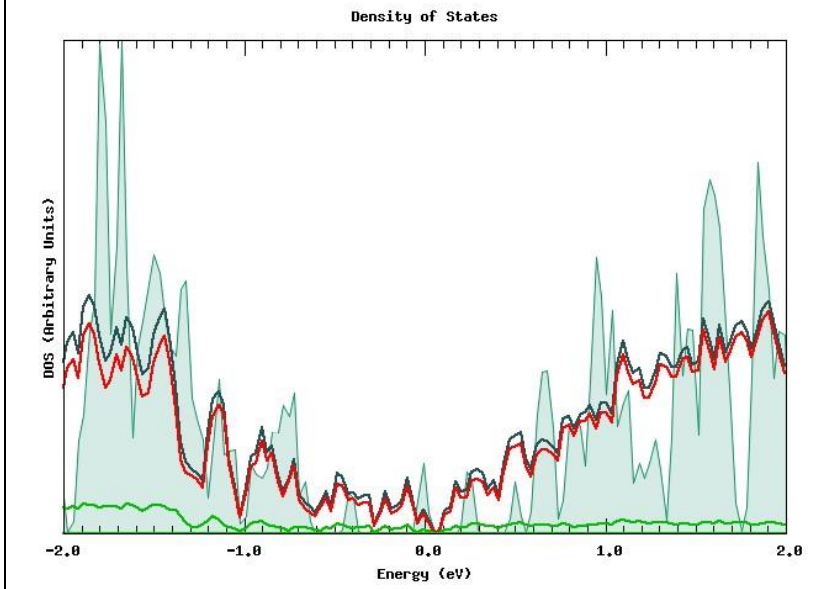

T-S-1

Triangular
Energy
0.63/2.83
NCu= 40
Nphos= 480
Psubst= 0
Relaxed cell
27.167
32.90
11.606

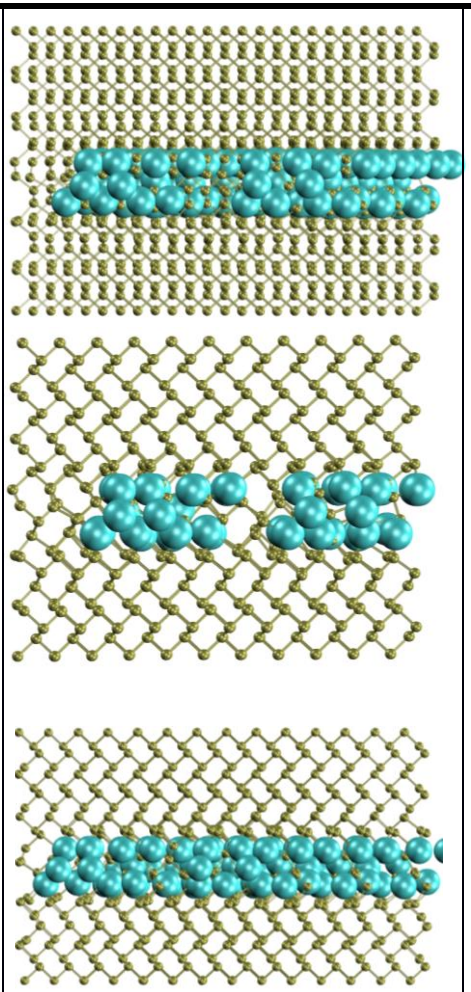

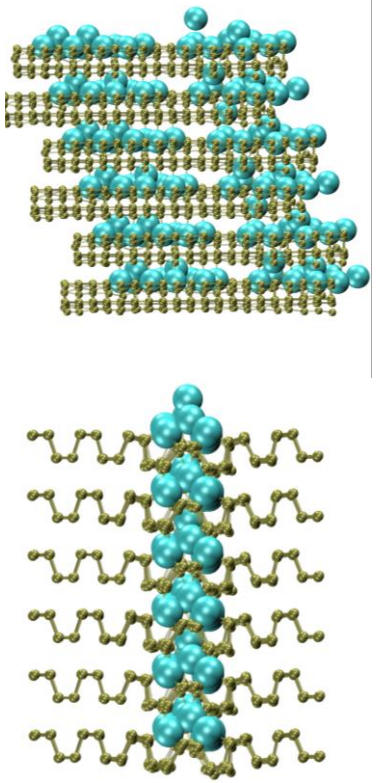

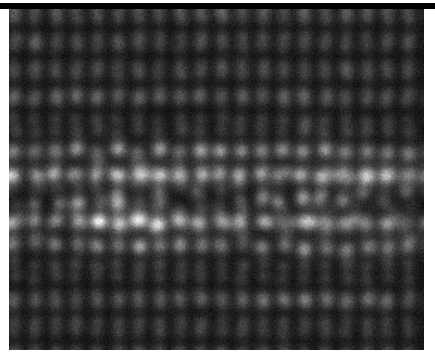

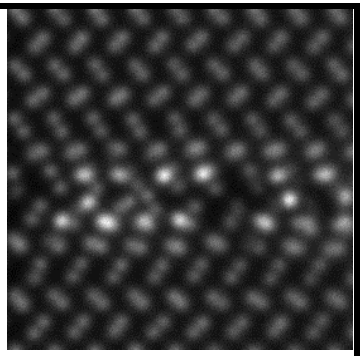

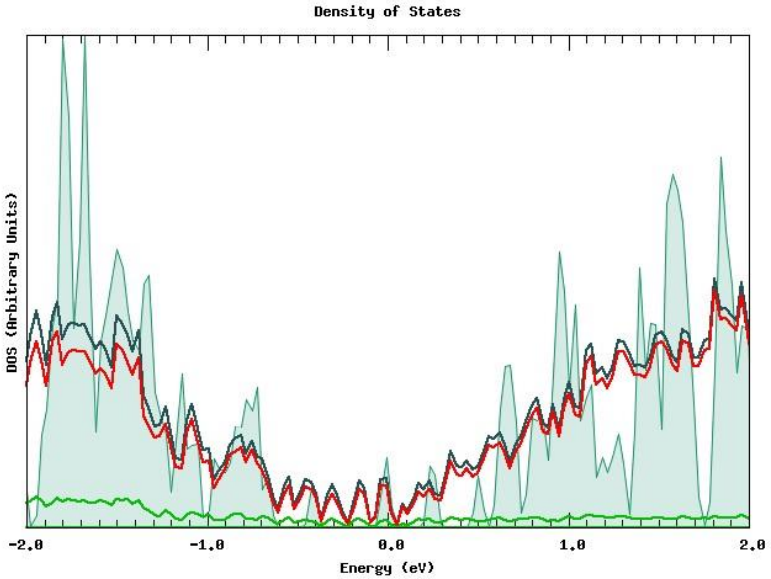

T-S-2

Triangular
Energy
0.63/2.81
NCu= 40
Nphos= 480
Psubst= 0
Relaxed cell
27.172
32.920
11.632

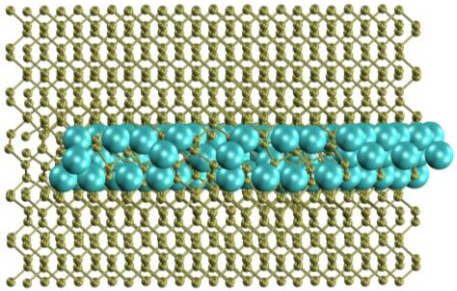

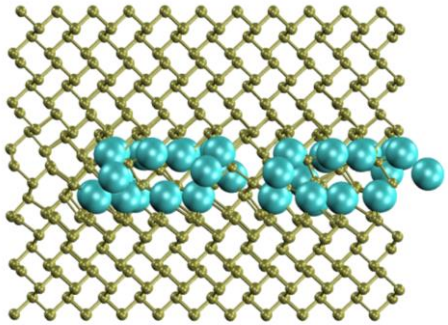

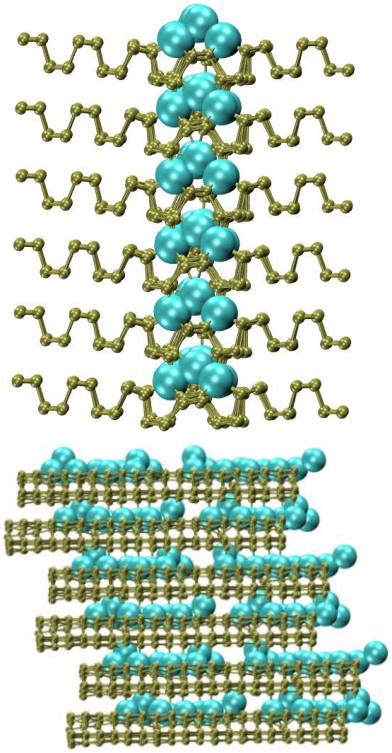

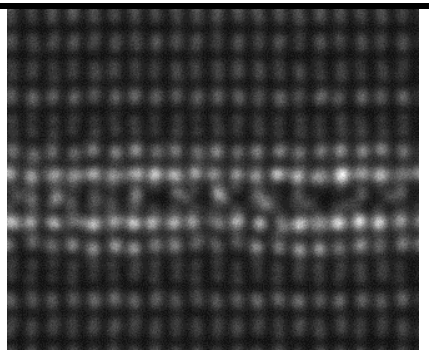

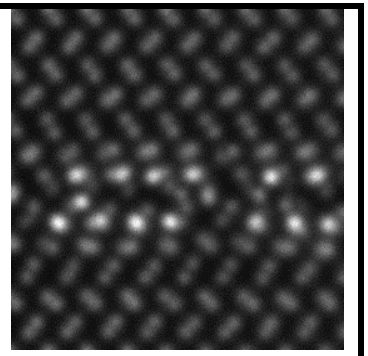

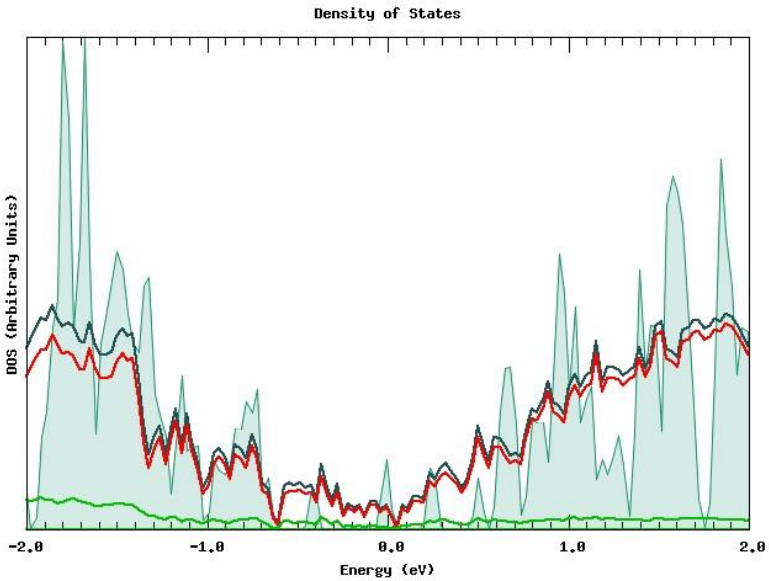

T-5

Triangular
Energy
0.63/2.79
NCu= 40
Nphos= 480
Psubst= 0
Relaxed cell
27.136
32.938
11.553

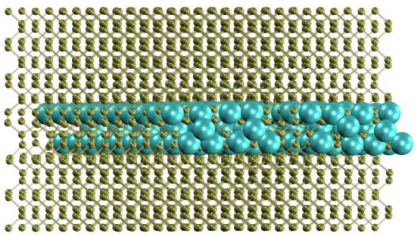

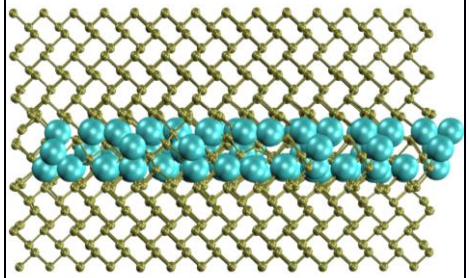

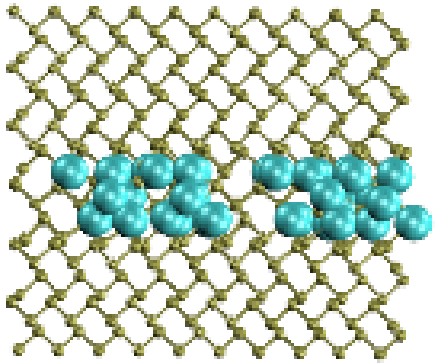

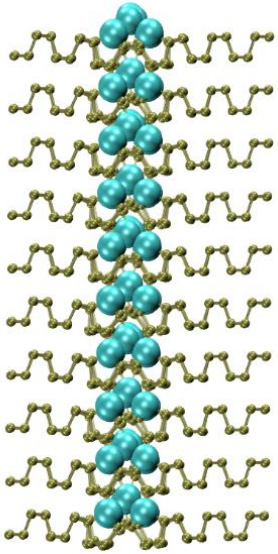

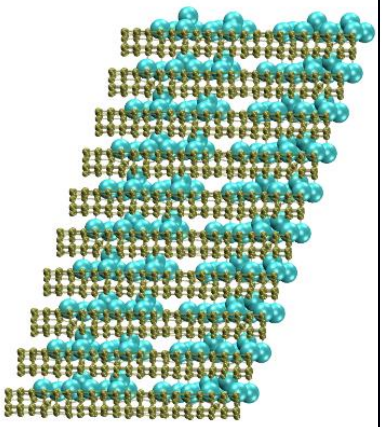

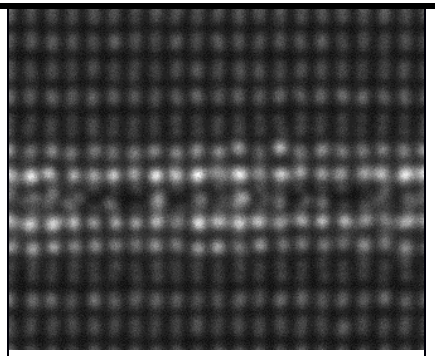

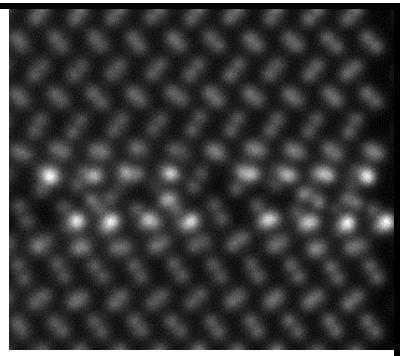

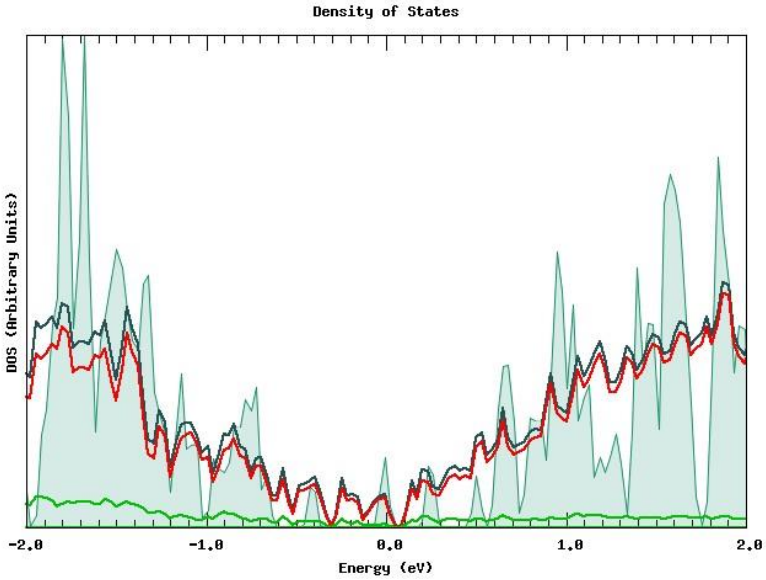

T-6

Triangular
Energy
0.60/2.70
NCu= 40
Nphos= 480
Psubst= 0
Relaxed cell
27.104
32.931
11.601

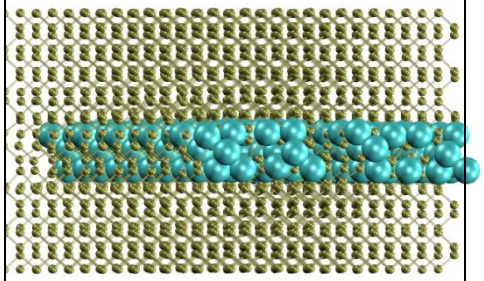

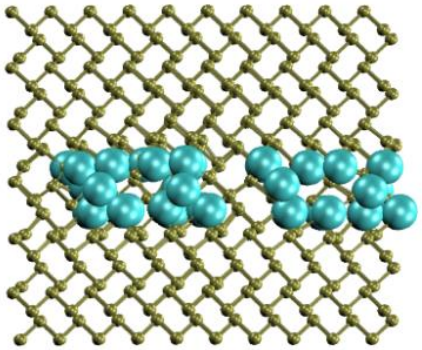

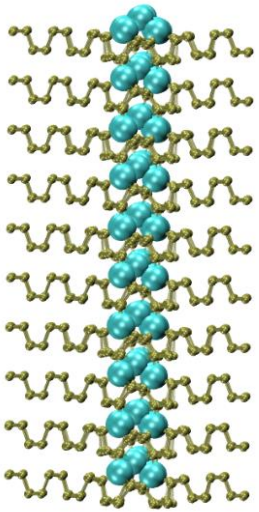

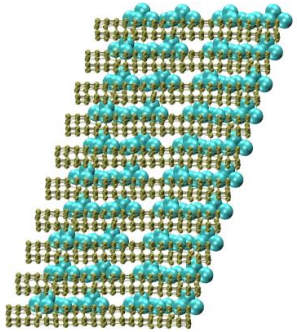

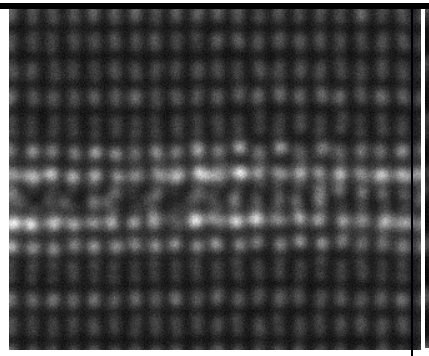

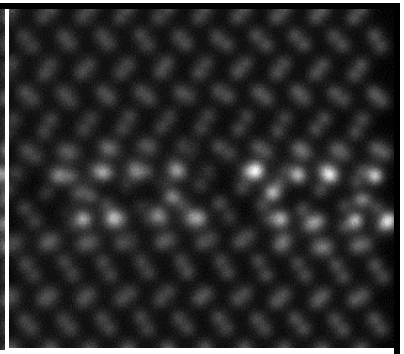

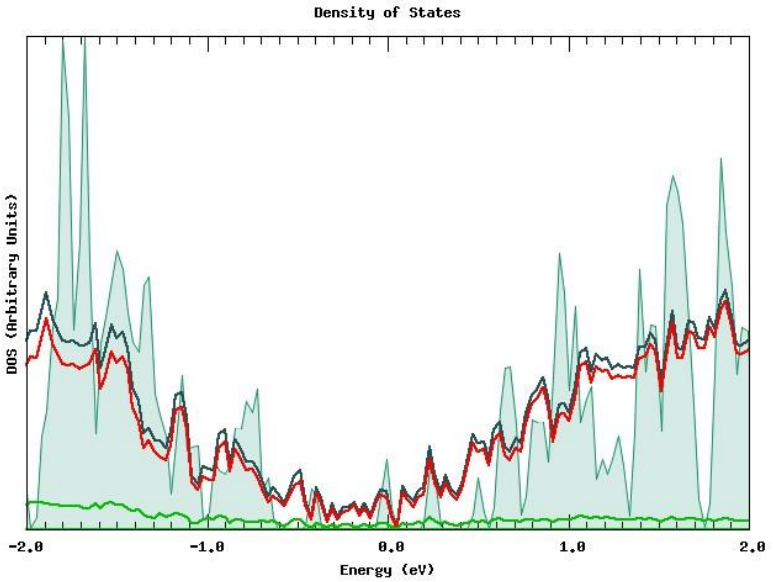

T-S-3

Triangular
Energy
0.60/2.69
NCu= 40
Nphos= 480
Psubst= 0
Relaxed cell
27.095
32.930
11.656

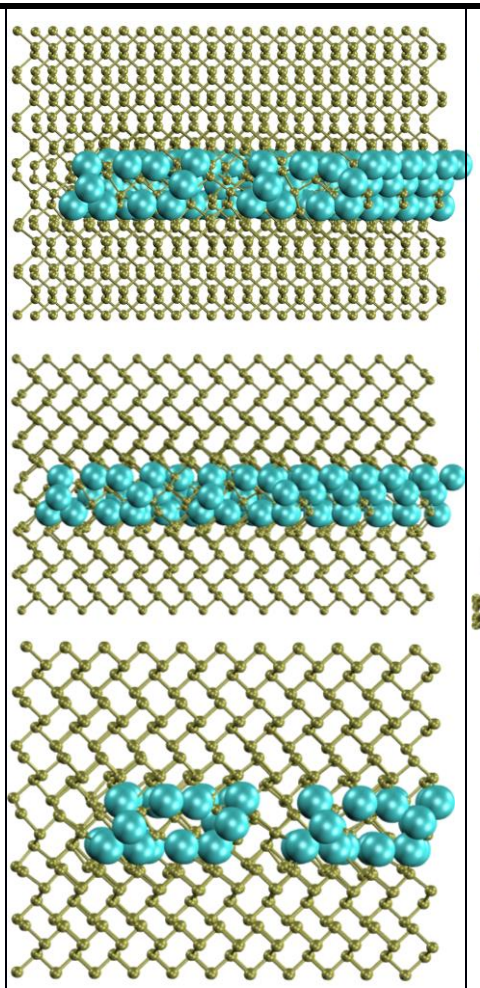

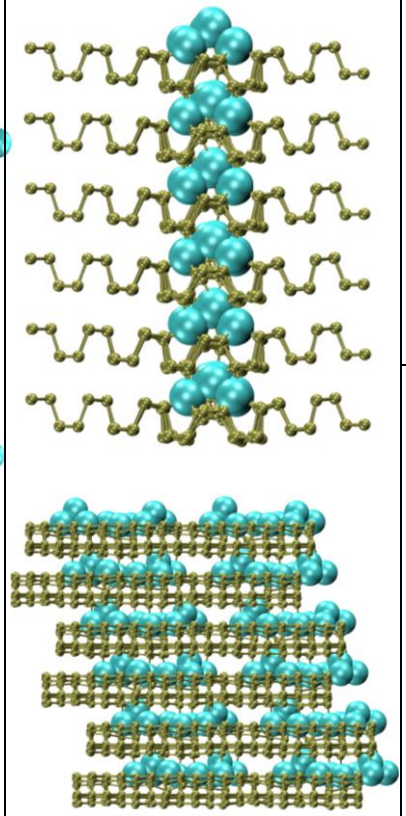

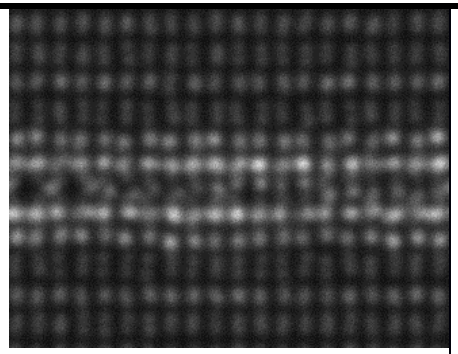

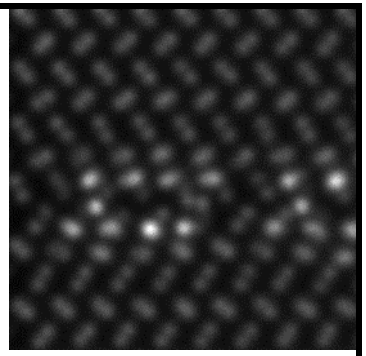

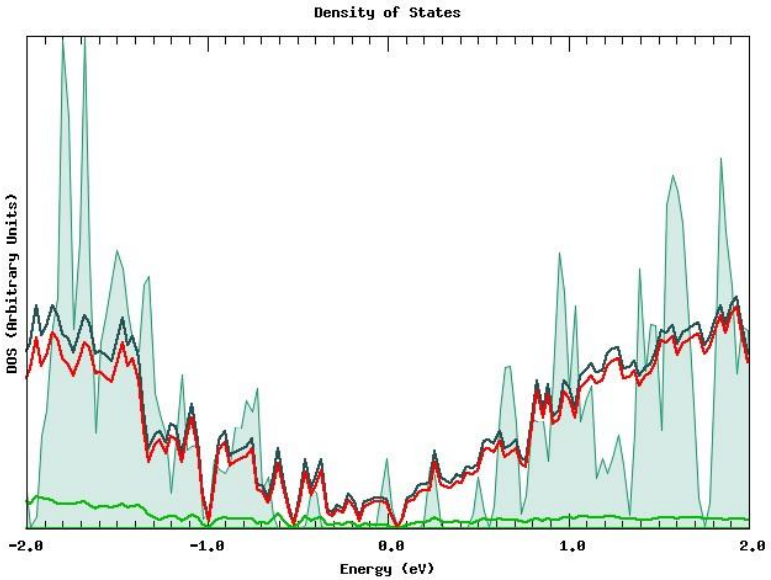

T-S-4

Triangular
Energy
0.60/2.68
NCu= 40
Nphos= 480
Psubst= 0
Relaxed cell
27.132
32.889
11.636

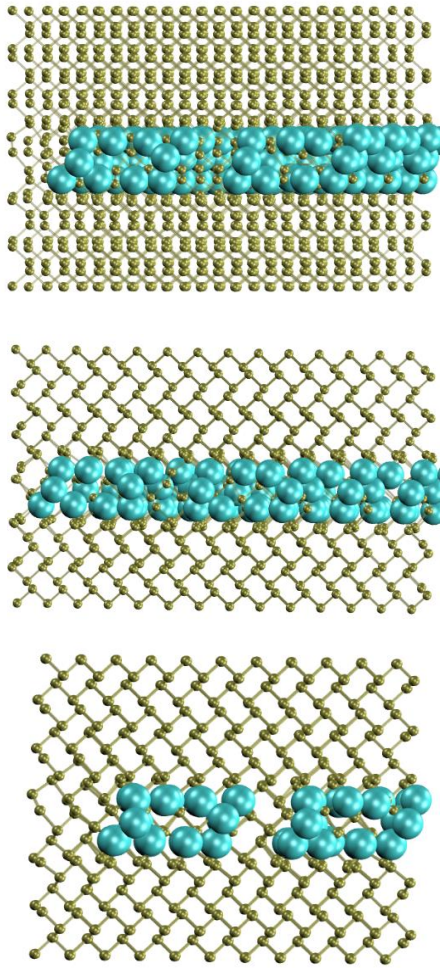

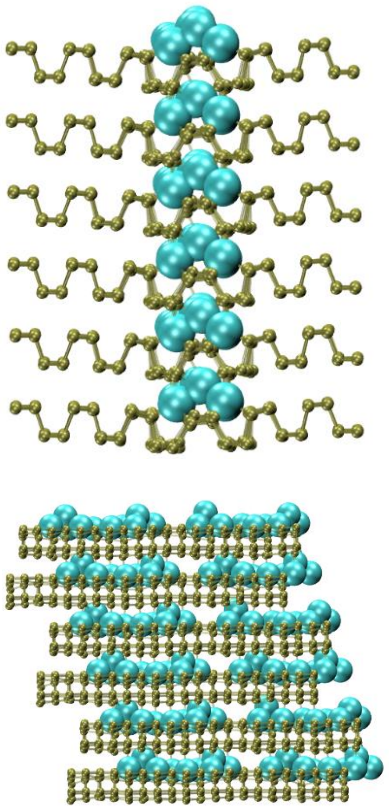

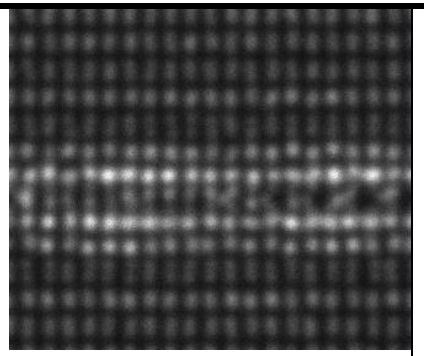

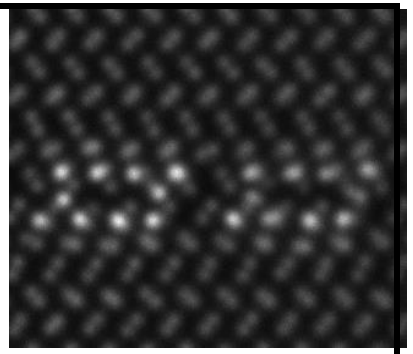

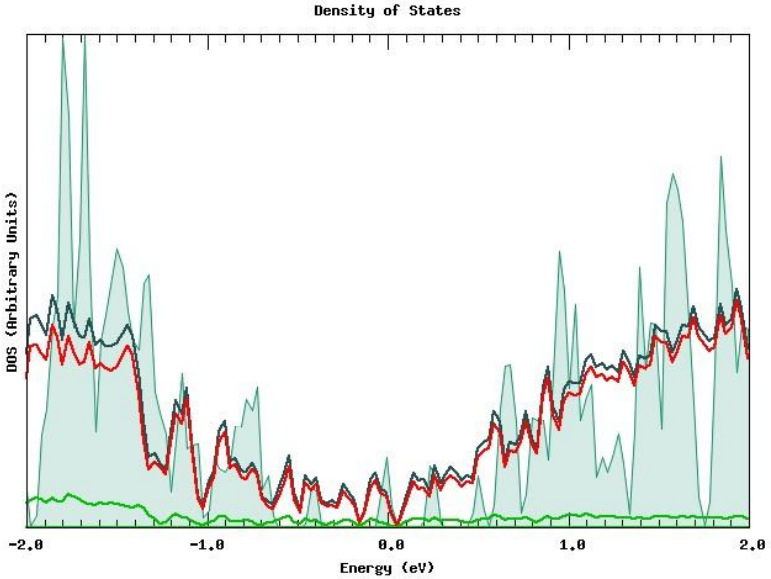

T-7

Triangular
Energy
0.58/2.87
NCu= 44
Nphos= 480
Psubst= 0
Relaxed cell
27.038
32.942
11.648

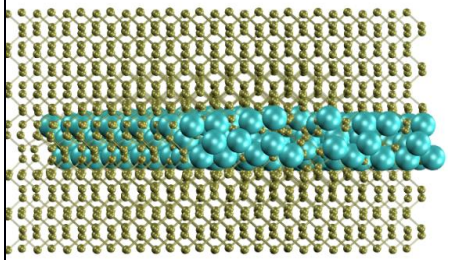

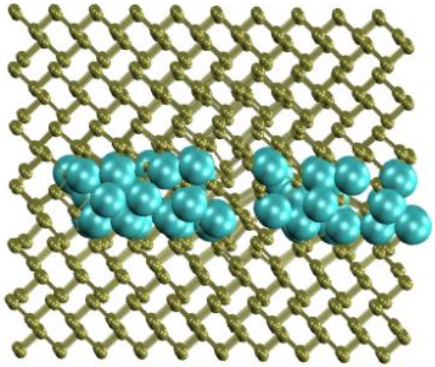

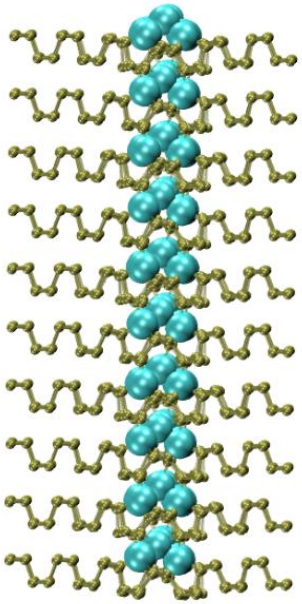

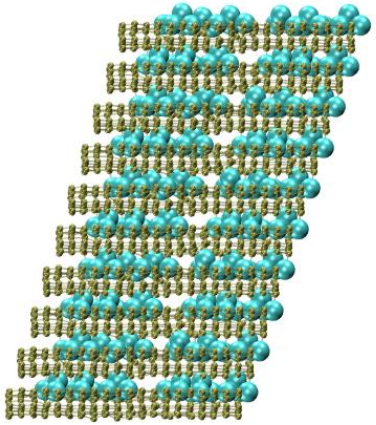

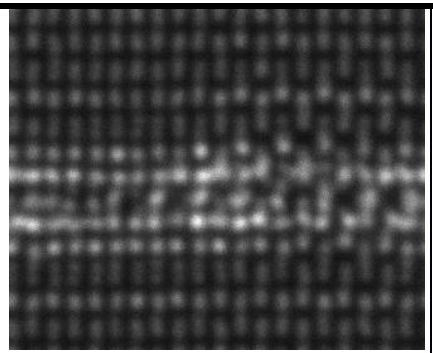

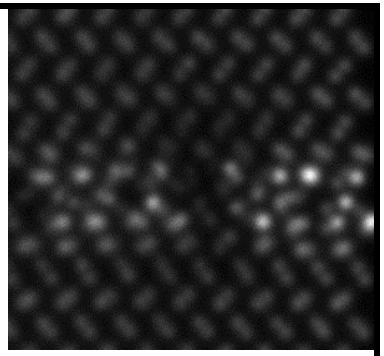

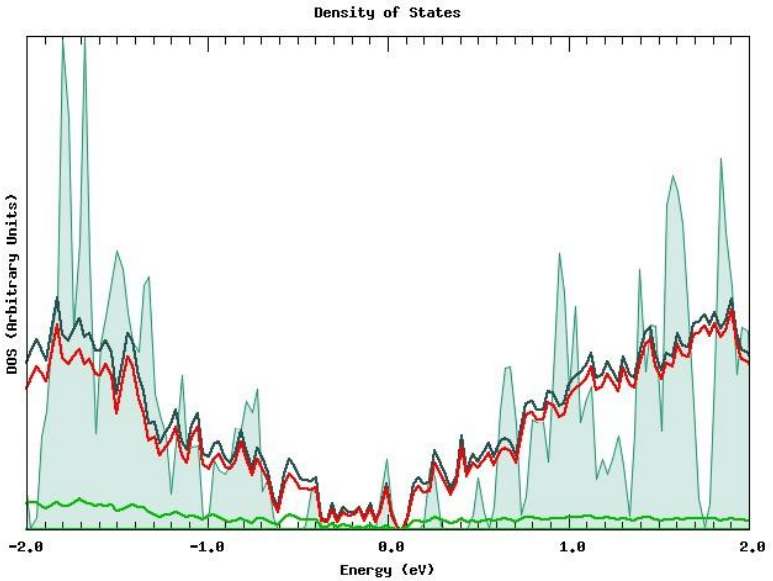

H-1

Hexagonal
Energy
0.51/2.30
NCu= 40
Nphos= 465
Psubst= 15
Relaxed cell
26.720
33.020
11.310

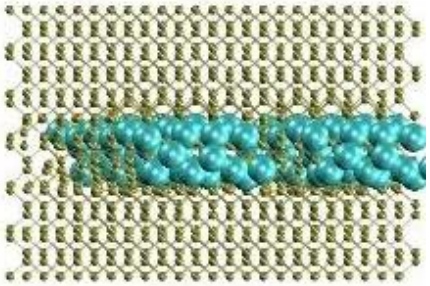

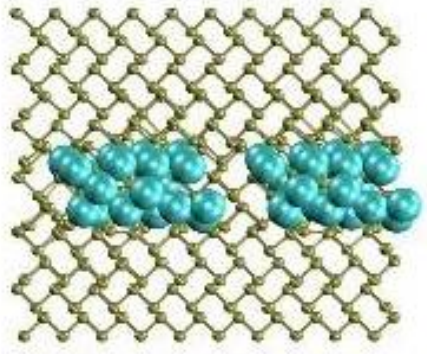

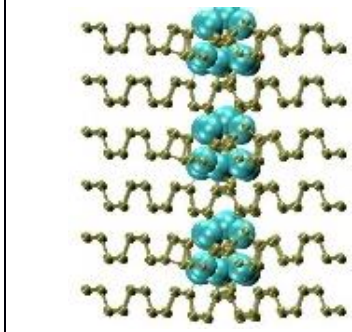

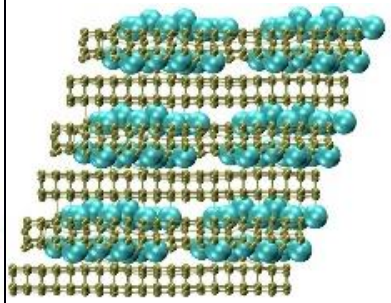

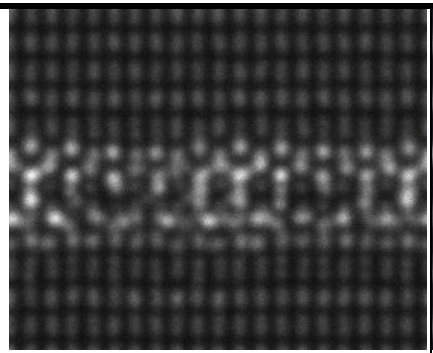

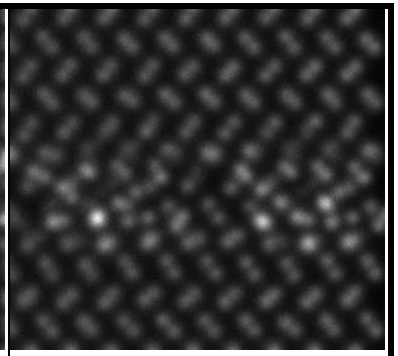

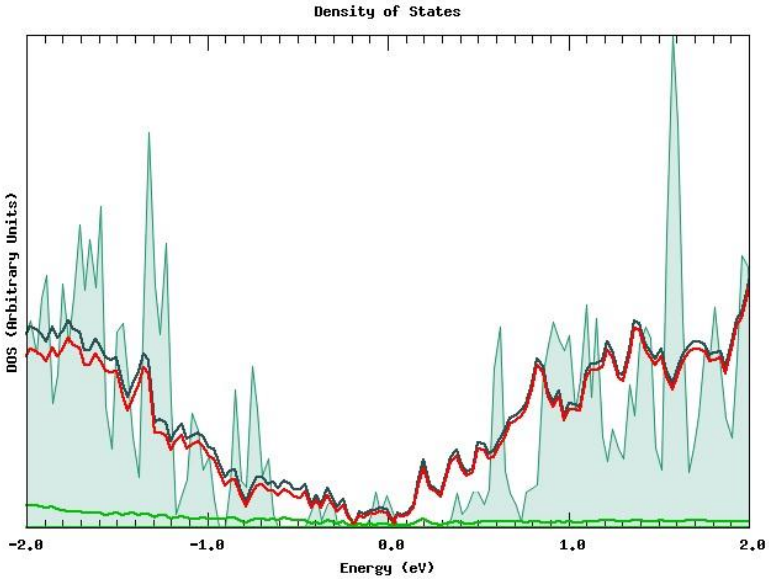

P-1

Pentagonal
Energy
0.26/1.12
NCu= 38
Nphos= 454
Psubst= 26
Relaxed cell
26.925
33.079
11.099 (10^-3)

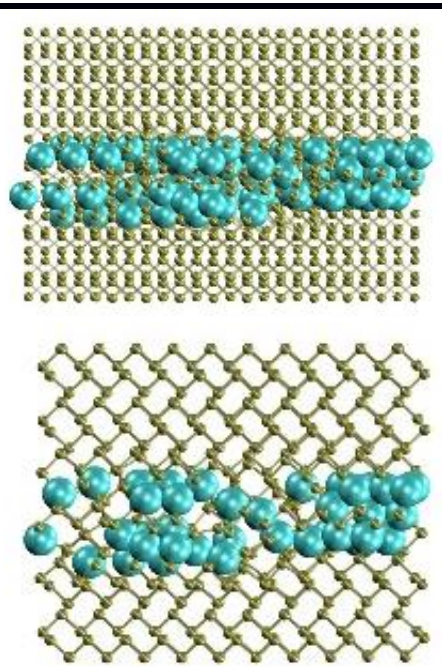

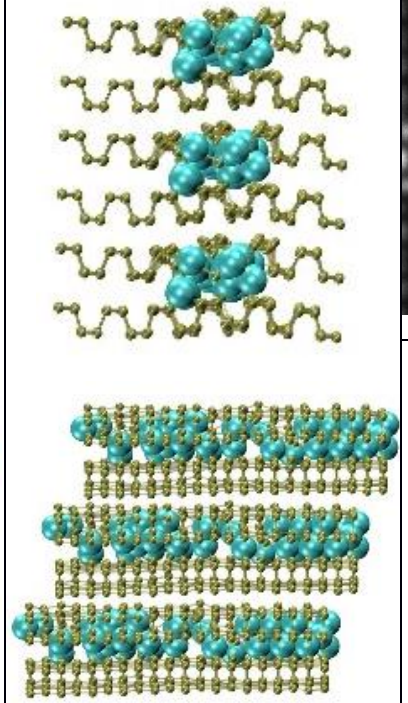

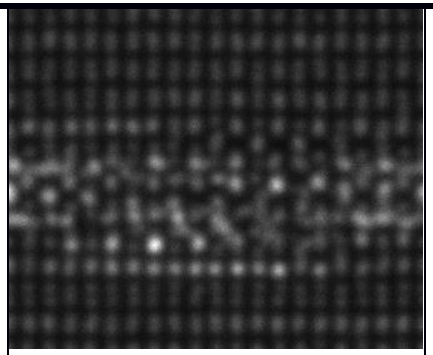

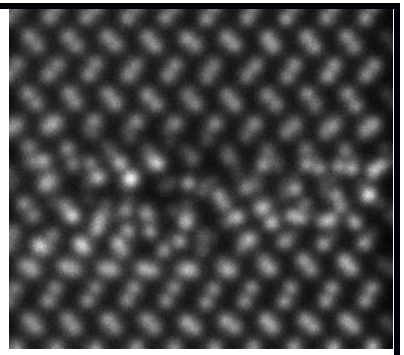

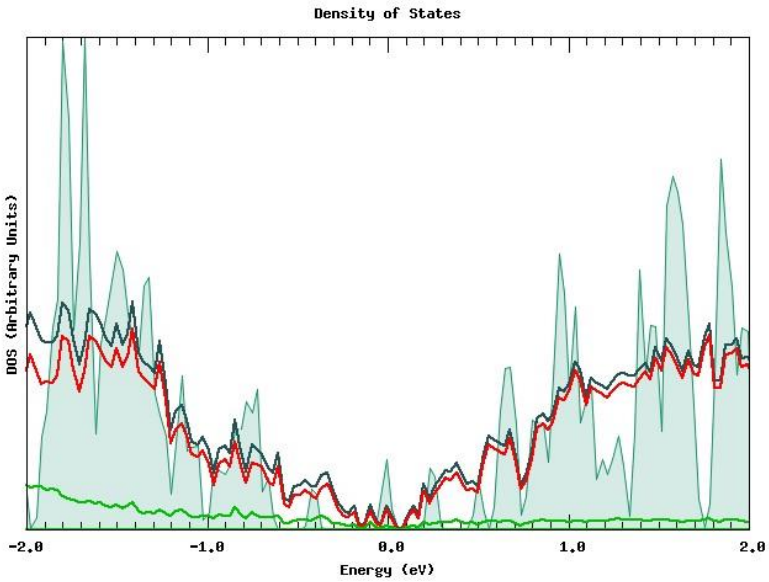

H-2_Trilay

Hexagonal
Energy
0.24/1.088
NCu= 40
Nphos= 705
Psubst= 15
27.099
33.044
16.526